Norwegian University
of Life Sciences

Master's Thesis 2023   30 ECTS
Faculty of Science and Technology

Exploration of LET dependent effects in proton beam therapy using machine learning analysis of TL glow curves from CaSO4:Tm and LTB:Cu

Erling Ween Eriksen
Environmental Physics and Renewable Energy

Exploration of LET dependent effects in proton beam therapy using machine learning analysis of TL glow curves from CaSO4:Tm and LTB:Cu

Erling W. Eriksen
Norwegian University of Life Sciences

(Dated: May 15, 2023)

Abstract

This thesis describes an investigation into the depth-dependent effects in proton radiation, evaluated by the use of Thermoluminescence Dosimetry (TLD) with CaSO4:Tm and LTB:Cu as target materials. Data collected on these target materials from experiments at Aarhus University and the University of Oslo with variable depth positions and dosages were preprocessed and inspected for general distribution and noise. The Linear Energy Transfer (LET) dependent Thermoluminescence (TL) response was investigated, showing a difference for intermediate energy protons between samples irradiated in the Bragg Peak and samples positioned early in the LET curve. A glow curve deconvolution was carried out, extracting TL parameters from the samples. Descriptive statistical features were also extracted from the samples. Statistical features, features extracted through deconvolution and raw glow curves were used to create predictive models of LET. Models based on Random Forest (RF), Principal Component Analysis (PCA) and Partial Least Squares (PLS) and Neural Networks (NN) were explored. Binary classification models gave satisfactory results between high and low LET with a validation/test accuracy of 0.93/0.87, and between samples irradiated in the Bragg peak and non Bragg peak with an validation/test f1-score of 0.96/1.0, while a reliable high precision regression model was not found.

Denne avhandlingen beskriver en undersøkelse av dybdeavhengige effekter i protonstråling, sett på ved bruk av termoluminescens dosimetri (TLD) med CaSO4:Tm og LTB:Cu som målematerialer. Data samlet inn fra eksperimenter ved Aarhus Universitet (AU) og Universitetet i Oslo (UiO) med posisjoner med varierende dybde og varierende dose ble preprosessert og inspisert for generell fordeling og støy. Termoluminescens (TL) signalets respons ble undersøkt i forhold til Linjær energioverføring (LET) som viste en forskjell for mellomenergi protoner for prøver som var bestrålt i Bragg-toppen og prøver som var plassert tidlig i LET-kurven. En dekonvolusjon av TL kurvene ble utført, der karakteristikker i form av TL-parametere ble ekstrahert fra prøvene. Enkel deskriptiv statistikk ble også brukt for å ekstrahere karakteristikker for prøvene. Statistiske karakteristikker, karakteristikker ekstrahert gjennom dekonvolusjon, og ubehandlet TL-data ble brukt til å lage modeller for prediksjon av LET. Modeller basert på Random Forest (RF), Nevrale Netverk (NN), Prinsipalkomponent Analyse (PCA) og Partial Least Squares (PLS) ble utprøvd med forskjellige data og karakteristikker. Prediksjon som binær klassifisering ga tilfredstillende resultater mellom grupper av høy og lav LET med en validerings/test nøyaktighet på 0,93/0,86 og mellom prøver bestrålt i Bragg-toppen og utenfor Bragg-toppen med en validerings/test f1-score på 0,96/1.0, mens en pålitelig regresjonsmodelldet ikke ble funnet.

CONTENTS

I. INTRODUCTION

Difficult to treat cancer is a major area of focus within the contemporary medical field. One growing technology is the treatment of localized tumors using proton beam radiation therapy [1]. To apply this method in the most beneficial way, minimizing the side-effects, one must have a complete understanding of the particle-tissue interactions present in treatment. One part of this is the determination of the characteristics of the deposited energy as a function of the depth of particle radiation penetration. Studying these effects in humans is both difficult and presents ethical dilemmas, and so model materials are often used as an analog to living tissue.

One method for this is using Thermoluminescence (TL), which is the phenomenon of radiation dependent, heat induced photon emission in some crystalline materials [2]. This effect has sporadically been discovered throughout history, with the first documented instance being an Italian shoemaker heating up Barite (BaSO4) containing impurities of copper trying to make gold, and instead creating a local attraction known as the glowing Bologna Stone [3]. It was in the first half of the 1900s that the intensive scientific study of these materials started, and where our current understanding of its physical mechanisms originated [4]. M. Curies doctoral dissertation in 1904 described the thermoluminescence of certain crystals after exposure to ionizing radiation [5]. Later Randall and Wilkins' work of 1945 laid the foundation of TL as an energy-band phenomena, where electrons and holes excited by radiation are trapped in imperfections of the crystal lattice structure, to be released by heat and measured as light [4][6].

The irradiated material offers useful information when heated and measured. This can be used to create beneficial technology, especially in the field of radiation protection and medicine. Arguably the most influential fact about thermoluminescence is that the emitted light is proportional to the cumulative dose of radiation received by the material[7]. This became the basis for reliable dose measurement devices for ionizing radiation which are still widely used today [2].

Thermoluminescence Dosimetry (TLD) has long been used for dosimetric measurements both in industry, radiation safety, and medicine [2], but taking these measurements further to create more comprehensive detectors, is still a nascent field. The ability to estimate additional qualities of radiation like Linear Energy Transfer (LET) based on measurements from widely used dosimeter equipment is useful in a number of ways, among them more precise measurements of biological damage caused by radiation treatment and dose estimations in space applications [8][9].

One emerging method of extracting more information from TL data is using machine learning. Machine learning has the potential to find unexpected patterns in data, and has recently been used to predict the time since radiation of TLD samples fairly accurately, as well as degradation in TL signal strength over time, called fading [10][11]. Expanding the application of ML techniques can be an opportunity to discover new information that is retained in the the TL process.

In this work, TLD readings from samples irradiated with protons will be analysed using machine learning techniques to attempt to extract information about depth dependent effects, focusing on LET, using samples from two markers, LTB:Cu and CaSO4:Tm. Firstly, relevant theory will be discussed, relating to TL as a physical phenomena, glow curve deconvolution and the relevant statistical and machine learning tools used for analysis and prediction. A description of the methodology used in analysis and model construction will then be presented, leading into the findings of exploring LET dependent effects in TLD, with an accompanying discussion.

II. THEORY

A. Thermoluminescence Dosimetry

Thermoluminescence dosimetry (TLD) is the practice of using materials that have a memory of ionizing radiation to estimate radiation dose and characteristics [7]. It is used in a variety of fields including medicine, radiation protection, geology and food production [2].

TLD uses crystalline insulators containing flaws that can act as traps for charge carriers that are excited by ionizing radiation [7]. These insulators retain a memory of incident ionizing radiation, which can be released by heating, radio-thermoluminescence, dissolving in another substance, radio-lyoluminescence or by UV irradiation, radio-photoluminescence [12]. Although the methods of releasing the information through photon emission from the materials differ, the mechanisms of storage remains the same [12]. This text will mainly concern itself with radio-thermoluminescence, hereby referred to as thermoluminescence or TL.

The memory of the ionizing radiation is created when the incident radiation on the materials excite some charge carriers from the valence band, either to the conduction band or to traps in the material, shown in the diagram in Figure 1. The carriers in the conduction band are more free to roam in the material, and have a certain probability of being trapped in the flaws in the material [7]. The simplest models, as the one used for the basis of dose measurement make significant assumptions, as long as they do not affect the dose measurements to a large degree. Some more complex, as the ones discussed later for deconvolution, try to approximate the real system more closely. Most of the following section on the physics of thermoluminescence is sourced from Handbook of thermoluminescence by C. Furetta , TLD Review part 1 by T. Kron and Thermally Stimulated Processes by R. Chen [13][2][7].

The fundamental quality of materials exhibiting thermoluminescence is the presence of traps and recombination centers between the valence and conduction bands of a material, illustrated in Figure 2. An electron trap is a metastable state from where an electron can be thermally excited to the conduction band [7]. A recombination center is a state containing hole, but which is too far from the valence band for an electron to be thermally excited to it [7]. In this case an electron can be excited to the conduction band and recombine with holes in the recombination center, but not the other way around. The mirror case is equally as likely, with holes in a trap and electrons in

a recombination center, with the trap close enough to the valence band for thermal excitation, and the electrons too far from the conduction band to be thermally excited [7]. A certain metastable state can therefore act as both a recombination center and a trap, depending on its distance to the valence and conduction bands.
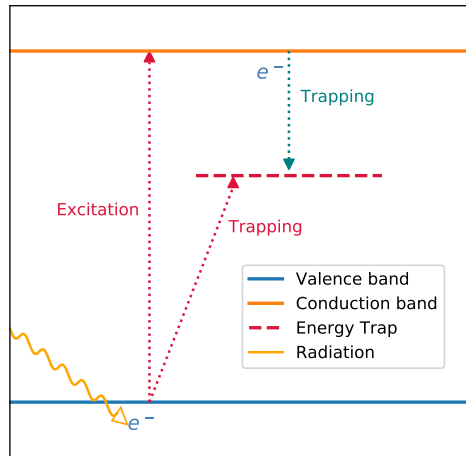

Figure 1: An energy band-gap diagram illustrating the Braunlich Scharman model of trapping of electrons (e^-) in a TL material [14].

After being irradiated, TLD samples are heated through a range of temperatures with a heating rate β, sometimes as slow as $0.5K/s$ for scientific applications, to $10K/s$ or higher for some industrial applications [2]. How much light is emitted from the recombination centers in the heating process illustrated in Figure 2, at what temperature, can be detected and is called the Glow Curve (GC) of a sample, which is the signal that is used for dosimetric and other applications[2]. A lower heating rate is used in scientific applications since the glow curve of a substance heated with a higher heat rate contains unwanted thermal effects making the glow curve more difficult to analyse [2].

The mechanism that drives the TL signal is the flow of electrons and holes in the material[7]. The electrons are trapped at a certain energy depth E, which is the difference between the energy level of the bottom of the conduction band and the trap. Each electron has a probability of escaping the trap by thermal excitation shown in Figure 2, expressed by

rate[7]. The total dose of a sample being heated from time $t = 0$ to $t = t$, with the initial state of no filled traps can be expressed as,

$$D = \int_N^n \frac{dn}{n}$$
$$= \int_0^t -A\frac{dD}{dt}dt \tag{4}$$

which gives the relationship between the population of traps and accumulated dose D as

$$n = N \times exp(-AD). \tag{5}$$

Considering the case where half the traps are filled, ie. $n/N = 0.5$, we obtain $A = \frac{0.693}{D_{1/2}}$ where $D_{1/2}$ Is the dose at which this is the case. Substituting Equation 5 into Equation 2 and taking the derivative, and using the expression for the probability of luminescence from Equation 1, we get an expression for the intensity of the luminescence of the sample at a certain temperature and dose, $I(D, T)$ as,

$$I(D,T) = -C\frac{dN_f}{dt}$$
$$= -C \times p \times N_f$$
$$= C \times s \times N\left[1 - exp(-AD)\right]exp(-\frac{E}{kT}) \tag{6}$$

which can be simplified when approximating $1 - exp(-AD)$ as AD for small values of D assuming $A \times D < 1$. This approximation has a maximal error rate of 36.8%, and limits the scope of valid doses, especially if $D_{1/2}$ is small. The simplified expression becomes

$$I(D,T) = C \times s \times N \times AD \times exp(-\frac{E}{kT}) \tag{7}$$

and shows that the intensity of the luminescence at a certain temperature T is proportional to the cumulative dose D, with proportionality constant C_p as

$$C_p = C \times s \times N \times A \times exp(-\frac{E}{kT}). \tag{8}$$

This is the defining property that allows these measurements to be used to determine the dose of a sample[2]. When having obtained this proportionality constant experimentally or otherwise, the measurement of dose to a fair degree of precision is elementary.
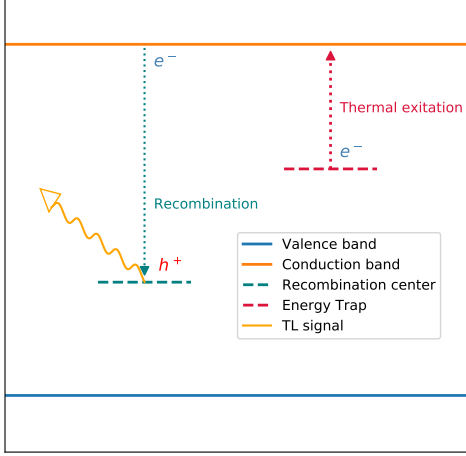

Figure 2: An energy band-gap diagram of the Braunlich Scharman model of heat induced excitation of electrons from a trap and recombination of electrons and holes in a recombination center in a TL material [14]. e^- are electrons and h^+ are holes.

the Arrhenius equation,

$$p = s \times exp(-\frac{E}{kT}) \tag{1}$$

where p is the probability of being excited to the conduction band, s is an insulator material constant, often presented as the frequency factor s^{-1}, E is as mentioned the trap depth, k is the Boltzmann constant and T is the temperature of the material [7]. When the electrons are excited to the conduction band from the traps, they have a probability of recombining with holes and thus causing the emission of a photon, illustrated in Figure 2. The places where this occurs are the recombination centers. Each material begins with a number of empty traps N, and as it is irradiated, N_f traps are filled, leaving n traps empty as

$$N_f = N - n. \tag{2}$$

The rate of decrease in unoccupied traps when a sample is heated can then be described as,

$$-\frac{dn}{dt} = A \times n\frac{dD}{dt} \tag{3}$$

where A is radiation susceptibility, which is specific to the material of the sample and $\frac{dD}{dt}$ is the dose

However, utilizing TL to gather more extensive information about the absorbed radiation, or the physical process itself, has shown to require a more comprehensive description of the TL phenomena. What model one chooses to use is based on what assumptions are most useful and necessary. For glow curve deconvolution, the goal is to decompose the glow curve into its underlying glow peaks [2]. For this case it is therefore useful to assume the glow curve as a superposition of glow peaks.

One model based on one energy trap and one recombination center scheme proposed by Schon in 1956 is the Braunlich Scharman model [14], illustrated in Figure 1 and Figure 2. It assumes that there are both holes and electrons as charge carriers and presents a set of four differential equations representing the flow of holes and electrons as a TL material containing trapped electrons is heated [13][14].

The first differential equation, Equation 9, governs the change of the concentration of electrons in the conduction band n_c

$$\frac{dn_c}{dt} = np_n - n_c A_n(N - n) - n_c m A_{mn} \quad (9)$$

where n is the concentration of trapped electrons and N is the concentration of electron traps, with p_n being the probability of the excitation of an electron from a trap to the conduction band. A_{mn} is the probability of an electron in the conduction band recombining in the recombination center, while A_n is the probability of the electron instead being retrapped in the electron trap. The equation

$$\frac{dn_v}{dt} = mp_p - n_v A_n(M - n) - n_v n A_{np} \quad (10)$$

governs the change in concentration of holes in the valence band n_v, where m is the concentration of trapped holes and M is the concentration of traps, with p_p as the probability of a hole being excited from a trap to the valence band and A_{np} is the probability of a hole recombining in an electron trap [7]. The final two equations

$$\frac{dn}{dt} = -np_n - n_c A_n(N - n) - n_v n A_{np} \quad (11)$$

and

$$\frac{dm}{dt} = -mp_p - n_v A_p(M - m) - n_c m A_{mn} \quad (12)$$

describe the change in concentrations of trapped electrons and trapped holes, respectively [7]. In the case that both recombination and transitions are radiative, the equation

$$\begin{aligned} I &= -\frac{dn_c}{dt} - \frac{dn}{dt} \\ &= n_c m A_{mn} + n_v n A_{np} \end{aligned} \quad (13)$$

describes the intensity I of the radiation during heating. Different assumptions of this model lead to different analytical equations for the intensity. Most of these assumptions are based on the the ratios describing the relationship between recombination and trapping probabilities are defined as

$$R_n = \frac{A_n}{A_{mn}} \quad (14)$$

for electrons and

$$R_m = \frac{A_p}{A_n p} \quad (15)$$

for holes [13]. There are five cases to consider that result in different models of the system[13]:

1) R_n and $R_m \approx 0$.

In this case retrapping is assumed to negligible for both holes and electrons, with the additional assumption that immobile trapped holes lead to the first order Randall-Wilkings model[6].

2) R_n and $R_m >> 1$.

Making assumption of immobile trapped holes, and assuming that recombination is negligible and retrapping is dominant leads to second order Garlick and Gibson equation[15] when assuming that there are no transitions of electrons to the valence band [13].

3) $R_n \approx 0$ and $R_m >> 1$.

In this case we assume negligible retrapping for electrons, while it is dominant for holes . This assumption also leads to the Randall-Wilkins model when assuming no transition of holes to the valence band [13].

4) $R_n >> 1$ and $R_m \approx 0$.

Assuming that holes are mostly retrapped and electrons are mostly recombined also leads to the first order Randall-Wilkings equation when assuming no electrons are excited to the valence band [13].

5) R_n and R_m are any number larger or equal to 0.

This is equivalent to not making any assumptions of the proportion, and so doses not lead to a simplified model.

From the preceeding differential equations, with the assumptions $n_c << n$ and $|\dot{n}_c| << |\dot{n}|$, the intensity, I is given as

$$I = -\frac{dm}{dt} \qquad (16)$$

$$= sn exp(-\frac{E}{kT}) A_m \frac{m}{A_m m + A_n(N - n)}$$

which was formulated by R. Chen as the basis for first and further order equations [7], but has also been presented by V. Maxia in an analysis of thermoluminescence using non-equilibrium thermodynamics [16].

These equations of thermoluminescence can then be applied with some assumptions to create models of the emitted intensity I of a TLD sample. A common assumption, that will be accepted for the proceeding models is the assumption of charge neutrality, $m(T) = n(T)$, that there are equal number of trapped holes and electrons in the material at any temperature. This stems from the assumption that before heating, the number of trapped holes and electrons in the material are approximately the same, and that under heating, their rates of release are equivalent [7]. Additionally, these models assume discrete, singular energy traps. This is a simplification of the real case of bands of energy levels [17].

Firstly, the first order kinetics model concerns itself with case (1) of negligible retrapping, meaning R_n and R_m approximately 0. From this assumption Equation 16 becomes,

$$I = sn \times exp(-\frac{E}{kT}) \qquad (17)$$

which with a constant heating rate β is solved as

$$I(T)$$
$$= sn_0 exp(-\frac{E}{kT}) exp\left[\frac{-s}{\beta} \int_{T_0}^{T} exp(-\frac{E}{kT'})dT'\right] [7].$$
$$(18)$$

This expression consists of two competing exponential factors, resulting in an early rise in intensity when the integral is small, and a rapid decrease in intensity when it grows sufficiently large. These two effects are attributed to the initial release of electrons from traps and the exhaustion of electrons/holes for recombination respectively [7].

Second order kinetics assumes case (2), where charge carriers are mostly re-trapped and only sometimes

manage to escape the cycle through recombination meaning R_n and $R_m >> 1$ [7]. Assuming that the material's traps are far from saturation, we get the expression

$$I = \frac{sR_n}{N} n^2 exp(-\frac{E}{kT}) \qquad (19)$$

with R_n along with other factors being identical as defined above. Although making the assumption of M. Curie, that retrapping and recombination are equally likely, the expression simplifies to

$$I = \frac{s}{N} n^2 exp(-\frac{E}{kT}) \qquad (20)$$

[5], showing that with this assumption, if re-trapping is radiative, we observe a higher intensity, due to any electron on average re-trapping many times. Equation 19 is solved for a constant heating rate as

$$I(T) = s'n_0^2 exp\left(\frac{-E}{kT}\right) \times$$
$$\left[\frac{s'n_0}{\beta} \int_{T_0}^{T} exp\left(\frac{-E}{kT'}\right) dT' + 1\right]^{-2} \qquad (21)$$

[7]. There are also models assuming a "mixed" behaviour between first and second order[7], where the assumption of $m(T) = n(T)$ is dropped, instead assuming

$$m = n + n_c + c \qquad (22)$$

where c is a constant and as before n_c and n are the electrons in the conduction band and traps respectively, along with m being the number of trapped holes. n_c is most commonly neglected, but with a real material, with defects and variations, $c = 0$ is dubious assumption since it is unlikely that the number of electrons and holes are precisely the same. In the case that $c \neq 0$, the equation

$$I = s'n(n + c)exp(-\frac{E}{kT}) \qquad (23)$$

arises from Equation 16, where s' is a constant with units $cm^3 sec^{-1}$ [7].

Attempting to account for TL cases where the order of n proportionality is not $\propto n$ or $\propto n^2$, a general order equation

$$I = s'n^b exp(-\frac{E}{kT}) \qquad (24)$$

was introduced in the early 1970, introducing the kinetic parameter b, with s' being a constant with units $cm^3(b-1)$[7]. The solution to this equation as a function of T is

$$I(T) = sn_0 exp\left(\frac{-E}{kT}\right) \times$$
$$\left[\frac{(b-1)s}{\beta}\int_{T_0}^{T} exp\left(\frac{-E}{kT'}\right)dT' + 1\right]^{\frac{-b}{b-1}} \quad (25)$$

for a constant heating rate β and is valid for $b \neq 1$ and $b \neq 2$ [7].

Although these equations are not expected to represent the physical reality of the system perfectly, as that depends on many more parameters $(n, m, Am, An, n, s$ and E from Equation 16), they have been shown to be at least mathematically sufficient to approximate a number of situations [7][12][13].

B. Glow Curve Deconvolution

Glow curve deconvolution is the practice of deconstructing the signal TLD curves into its subcomponents to study the physical properties of the energy traps of the material. The intensity models presented in Equation 18, Equation 21 and Equation 25, are based on different assumptions, but share an important commonality, they cannot be solved analytically [18] [2]. This creates the challenge of applying the models to real data, and the opportunity for a variety of suggested numerical solutions and/or assumptions. One common way is to use numerical optimization to fit the intensity models to experimental data, to attempt to extract the unknown parameters of the model [2].

One set of equations, based on the descriptions of R. Chen [7], are the equations proposed by G. Kitis et. al. in 1998 [18]. The three suggested equations correspond to the first, second and general order kinetics, and aim to describe a glow peak corresponding to a single energy trap, of which a glow curve can consist of many. The first order equation is given as

$$I(T) = I_m exp\left[1 + \frac{E}{kT}\frac{T-T_m}{Tm} - \frac{T^2}{T_m^2}\right.$$
$$\left.\times exp\left(\frac{E}{kT}\frac{T-T_m}{T_m}\right)(1-\Delta) - \Delta_m\right] \quad (26)$$

with $\Delta = 2kT/E$ and $\Delta_m = 2kT_m/E$, where I_m is the peak intensity, T_m its corresponding temperature,

E is the energy gap from the valence band to the trap, T is the temperature and k is the Boltzmann constant. Intensity for kinetics of the general order are described as

$$I(T) = I_m b^{\frac{b}{b-1}} exp\left(\frac{E}{kT}\frac{T-T_m}{T_m}\right) \times \left[(b-1)(1\right.$$
$$\left. - \Delta)\frac{T^2}{T_m^2}exp\left(\frac{E}{kT}\frac{T-T_m}{T_m} + Z_m\right)\right]^{-\frac{b}{b-1}} \quad (27)$$

where $Z_m = 1 + (b-1)\Delta_m$ and b is the kinetic parameter [18]. Kinetics of order 2 is described as,

$$I(T) = 4I_m exp\left(\frac{E}{kT}\frac{T-T_m}{T_m}\right) \times \left[(1\right.$$
$$\left. - \Delta)\frac{T^2}{T_m^2}exp\left(\frac{E}{kT}\frac{T-T_m}{T_m} + Z_m\right)\right]^{-2} \quad (28)$$

which can be reached by substituting 2 for b in Equation 27. Knowing the unknowns in these equations for a substance, one can simulate the glow curve, or having glow curves, one can try to estimate the unknowns to learn something about the material or how it has been irradiated [2].

Most glow curves consists of multiple peaks. It is therefore often necessary to combine the equations as a superposition

$$I(T) = I_1(T) + I_2(T) + ... + I_N(T). \quad (29)$$

There are also ways to estimate parameters using a variation in heating rates and the Arrhenius equation (Hoogenstraads method), although it is deemed somewhat unreliable, is constrained to first order peaks and requires data with varying heating rates [19]. It is also possible to calculate E and b using the integral of the curves (Three point method), but this require a curve that starts and ends at 0 and has a singular or isolated peak [20].

Since measured glow curves often lack the requirements of these simpler methods, a common and general method of estimating the parameters of a glow curve is using curve fitting using an objective function [2]. An objective that is often used is the minimization of the squared difference between the analytic expression and the experimental datapoints known as the residual sum of squares (RSS),

$$RSS = \sum_{i}^{N}[y_i - \hat{y}_{i,p}]^2 \quad (30)$$

or the RSS weighted by the measurement uncertainty at each point σ_{y_i}, giving the chi-squared error criterion,

$$\chi^2 = \sum_i^N \left[\frac{y_i - \hat{y}_{i,p}}{\sigma_{y_i}} \right]^2 \tag{31}$$

where in both cases N is the number of datapoints, y_i is each experimental intensity at a certain temperature, $\hat{y}_{i,p}$ is the intensity calculated with the current glow curve parameters p using the intensity function of the glow curve. For a measure of the error of the fit that has the same units as the original function, the Root Mean Squared Error (RMSE) is given as

$$RMSE = \sqrt{\frac{\sum_i^N [y_i - \hat{y}_{i,p}]^2}{N}}. \tag{32}$$

Another common metric often used in the fitting of spectral data is the Figure Of Merit(FOM), given as

$$FOM = \frac{\sum_{i=1}^N |y_i - \hat{y}_i|}{\sum_{i=1}^N |y_i|}[21]. \tag{33}$$

Another metric often used for curve fitting is the coefficient of determination, know as R^2, expressed as

$$R^2 = \frac{RSS}{\sum_{i=1}^N (y_i - \overline{y})^2} \tag{34}$$

[22]. For RSS, RMSE and FOM, the value is minimized, for the R^2 the value is maximized up to a value of 1, while for the chi-squared criterion the object is to approach as close as possible to 1, where a lower value signifies overfitting [23]. FOM, made by Balian, H. G. et al. as an improved metric for fitting curves in gamma ray spectroscopy, tandard practice requires an FOM of below 0.025 to consider at curve fit as good, and below 0.035 to be considered flawed but decent [21] . In more recent studies applying glow curve deconvolutions, a value lower than 0.05 can sometimes be considered an acceptable fit [18]. Once one has found a fitting objecting function for the problem, there are many algorithms to choose from to attempt to fit the curve with the right parameters.

C. Levenberg-Marquardt

One algorithm often used for curve fitting Levenberg-Marquardt (LM) is a numerical algorithm developed in the 1960's for approximation of non-linear least squares problems. The LM algorithm consists of two subroutines: Gradient descent and the Gauss-Newton method. When the parameters are far from the optimum, the objective function has a large loss, the LM algorithm is most like gradient descent [24]. When it approaches the optimal solution, it acts most like the Gauss-Newton method[24]. An overview of the method will be given below, for a more detailed mathematical description of the Levenberg Marquardt method see H.P Gavin [24] or A. Björck's book on numerical least squares problems[25] .

Gradient descent works by calculating the gradient of loss in a parameter space. By calculating the way to increment the parameters that is worst at decreasing the chosen loss function, the algorithm can increment the parameters in the opposite direction, aiming to gradually improve the fit. The update of the parameters δ_{gd} are calculated as

$$\delta_{gd} = \alpha \mathbf{J}^T \mathbf{W}(\mathbf{y} - \hat{\mathbf{y}}) \tag{35}$$

where α is the step length, y is the experimental value and $\hat{y}$ is the current estimate, $\mathbf{W}$ is the weighting matrix, which can be adjusted for specific goals, but is commonly diagonal with

$$\mathbf{W}_{ii} = \frac{1}{\sigma_{y_i}^2} \tag{36}$$

where J^T is the transpose of the Jacobian, where $J = \frac{\partial \hat{y}(p)}{\partial p}$. The new parameters are then updated to

$$\beta_{k+1} = \beta_k + \delta_{gd,k} \tag{37}$$

where k is the iteration step.

The Gauss-Newton method works by iterating on an initial guess of the minima of the cost function, and then using a Taylor expansion to attempt to converge to the true minima[24]. It does this using the assumption that the objective function of the parameters is locally quadratic, simplifying the attempt to converge to a minima [25]. The first-order Taylor series expansion describing the increment is

$$\hat{\mathbf{y}}(p + \delta_{gn}) \approx \hat{\mathbf{y}}(\mathbf{p}) + \left[\frac{\partial \hat{\mathbf{y}}}{\partial \mathbf{p}} \right] \tag{38}$$
$$= \hat{\mathbf{y}} + \mathbf{J}\delta_{gn}$$

and can be substituted into the objective function, where δ_{gn} is the parameter update each iteration step. The optimal parameter update is when $\frac{\partial \chi^2}{\partial \mathbf{h}} =$

0, resulting in an expression for the update of the parameters as

$$\left[\mathbf{J}^T\mathbf{W}\mathbf{J}\right]\delta_{gn} = \mathbf{J}^T\mathbf{W}(\mathbf{y}-\hat{\mathbf{y}}) \qquad (39)$$

where again $\mathbf{W}$ is the weight matrix, and $\mathbf{J}$ is the Jacobian, while $\mathbf{y}-\hat{\mathbf{y}}$ is the residue of the fit. The Levenberg-Marquardt algorithm is a combination of these two routines, given as the expression

$$\left[\mathbf{J}^T\mathbf{W}\mathbf{J} + \lambda\mathbf{I}\right]\delta_{lm} = \mathbf{J}^T\mathbf{W}(\mathbf{y}-\hat{\mathbf{y}}) \qquad (40)$$

where δ_{lm} is the update to the parameters, $\mathbf{I}$ is the identity matrix and λ is the dampening parameter [24]. It is the left side of equation that modulates between the Gauss-Newton and Gradient Descent. A larger value of λ causes the update to be closer to gradient descent in Equation 35, while decreasing the value causes more similar update to Gauss Newton in Equation 39. λ is initialized to be a large number, and then decreased as the solution becomes better, resulting in the convergence towards the Gauss-Newton method as the algorithm converges to a minima. The algorithm stops iterating when either the gradient of the objective function is below a defined threshold, the change in parameters is below a certain threshold or when the objective function has reached its targeted performance [24].

An excellent implementation of the Levenberg-Marquardt algorithm is in the `Python` package `lmfit`, developed at MIT by Matt Neville et al. [26]. This is also the tool that will be used for glowcurve deconvolution in this work.

D. Radiation energy and LET

When applying radiation treatment in-vivo to patients, safety is of utmost importance. One part of this is understanding radiation quality and how much tissue damage is caused by the treatment. With the advent of new types of radiation treatment, like proton therapy, the methods for evaluating what dose to administer must be reinvestigated to assure minimum harm.

The same dose of different types of radiation can cause different amounts of damage to the target area, dependent on factors like particle energy, atomic number and tissue types [27]. One measure of the efficiency of a radiation type is the Relative Biological Effectiveness (RBE), calculated as

$$RBE = \frac{D_{X-ray}}{D_{test}} \qquad (41)$$

[27] where D_{X-ray} is the Dose of $250KVp$(KiloVolt peak) X-rays required to produce a certain biological effect, and D_{test} is the amount of another type of radiation required to produce the same biological effect.

Linear Energy Transfer (LET) is a measure of the deposited energy of a radiation beam per unit of the beam's path [27]. It differs between the type of radiation and target material , as well as with depth [REF]. Calculating LET for more complex materials is very difficult and often requires detailed numerical solutions in the form of simulations [28].

LET measurements can help researchers understand the quality of radiation, leading to more precise treatment for patients [29]. If it is possible to measure LET with TLD, then that opens opportunities for beam experimentation outside of in-vivo and in-vitro experiments. It could also improve dosimetry, as LET can be an important factor for estimating some aspects of real biological damage [8][29].

To estimate the depth dependent distribution of LET, it is possible to use openly available software like FLUKA [28]. This method has been shown to yield relatively precise results, finding the values for water to be within 10% of comparable experimental data collected with a parallel plate ionization chamber [30]. Since tissue is an inhomogenous substance consisting of many elements with different atomic numbers, making it harder to model, exhibiting a difference to water that varies with radiation type [31].

E. Thermoluminescence Materials

Materials used for thermoluminescence are isolators with the capability of containing stable traps for charge carriers, whether intrinsically or through doping of another substance[7].

Two different materials that can be used for TLD experiments are Lithium tetra borate (LTB, Li24B4O7) doped with copper(Cu) and Calcium Sulfate (CaSO4) doped with Thulium (Tm). This thesis uses data collected from samples of both of these, in the form of nanoparticles prepared in the form of pellets.

1. LTB:Cu

LTB doped with copper (LTB:Cu) is a dosimetry material first synthesized in 1980 by M. Takenaga et al. as a promising TLD material, with minimal signal fading over time and high sensitivity [32][33]. LTB:Cu has an effective atomic number of 7.3, which is similar to the average atomic number for human tis-

sue, making it a good model for radiation absorption [13].

From TLD and spectroscopy analysis of LTB:Cu irradiated with gamma radiation and x-rays, LTB:Cu has shown TLD intensity dependent on the mass of the pellets used, likely based of heat transport and radiation interaction [34].

An important quality of a TL material is the structure of its glow curve [2]. The original synthesis process by Takanaga et. al. using a sintering method, as well as descriptions by C. Furetta indicate two peaks in the LTB:Cu glow curve [33][13]. Later studies of LTB:Cu has shown varying peaks in its glow curve based on radiation, showing a superposition of four peaks for gamma radiation and two distinct peaks for x-rays [34]. Two peaks have also been observed for beta radiation of single-crystal LTB, where a glow curve deconvolution gave two peaks with an order of kinetics of approximately 1 [35].

Another recent study of LTB:Cu synthesized with a combustion process has also shown a more complex glow curve exhibiting 4 peaks [36], showing that the choice of synthesis affects the properties of the material. This is also illustrated by Soheilan et al. when comparing three different synthesis methods of LTB:Cu, there was a significant variance in glow peak distribution and sensitivity based on preparation [37]. This creates a challenge when comparing the results of one experiment to another, since most preparations are slightly different.

2. CaSO4:Tm

CaSO4 doped with Thulium (CaSO4:Tm) was first developed by Yamashita et al. in 1971 in an attempt to create a TLD material with high sensitivity, low signal fading and a simple glow curve [38]. In its first investigation its only drawback seemed to be that it did not have a tissue equivalent effective atomic number, although it was comparable to that of bone. CaSO4:Tm is used widely and exhibits a stable glow peak at about 220°C that is often used for dose estimations [39].

The original synthesis of CaSO4:Tm showed similar TLD properties as CaSO4 doped with dysprosium, with one major glow peak at around 220 °C, and two small shoulders at approximately 80 °and 120 °. While at higher doses, around a few Gy, an additional peak at 250 °was present [38].

F. Predictive modeling and machine learning

This section will briefly describe the methods applied in this thesis. More comprehensive descriptions of predictive modeling and machine learning can be found elsewhere, among them Python Machine Learning by Raschka, S. et al. [40].

One way of understanding predictive modeling is viewed as an extraction of patterns from data to create functions that output some value of interest. Given some input of size $N \times M$, where there are N samples and M features, the model aims to predict a set of variables for each sample, resulting in an output of size $N \times K$ where K is the number of target variables that the model is trying to predict for each sample. This is equivalent to creating a function $f(\vec{x}) = \vec{y}$, where $\vec{x}$ is one sample represented by M features and $\vec{y}$ is a prediction vector of the K variables of interest. Regression models can be described as functions where the prediction vector $\vec{y}$ contains continuous values that can be any number, while classification models can be described as functions where the prediction vector $\vec{y}$ contains discrete values, describing the category into which the sample is classified. Assuming that there is a real function that describes the relationship between the features of the samples $\vec{x}$ and the variables of interest $\vec{y}$, the essential part of predictive modelling is to create a function that approximates the real function as closely as possible.

1. Principal Component Analysis and PCR

Principal Component Analysis (PCA) is a method for analysing the variance of a dataset across features, finding uncorrelated multidimensional latent features that contain maximal variance[41]. These new features are a combination of the original features, and can often simplify the dataset by reducing dimensionality while attempting to preserve as much information as possible [41]. The new constructed features are named PC1, PC2 and so forth, where PC1 is the dimension of maximal variance and following dimensions are orthogonal to the original and capture less variance. Principal Component Regression (PCR) uses PCA to reduce the dimensionality of the dataset, and then completes a linear regression to estimate the target variable [42].

2. PLSR

Partial Least Squares Regression (PLSR) like PCR, is a regression method based on analysing the variance

in the data [43]. The main difference between PCR and PLSR is that PLSR uses the target variable to account for the predictive power of the newly generated latent variables [43]. This means that PLSR often requires fewer dimensions to reach the same predictive power[44].

3. Random Forest

The Random Forest (RF) algorithm is a shallow, supervised, ensemble machine learning algorithm that is used to predict a target variable from a set of data [40]. It consists of simpler parts, called decision trees that linearly classify the data by creating decision boundaries along different features. Many decision trees are then combined to create a multidimensional decision boundary to estimate the target variable [40]. RF algorithms exist for both classification and regression.

4. Neural Networks

Neural Networks are deep machine learning algorithms that consist of neurons connected in a network that propagates information to attempt to complete a multitude of tasks. First created as an attempt to emulate how the network of neurons in the human brain solves complex problems, neural networks have over time been implemented to solve a wide variety of tasks [40]. A neural networks consists of layers of nodes, where there is one input layer and one output layer, as illustrated in Figure 3. The input layer has a number of nodes equal to the number of features of each sample $\vec{x}$, and the output layer has a number of nodes equal to the number of variables in the target vector $\vec{y}$. The hidden layers consist of nodes that serve as connections in the propagation of information, denoted by arrows in Figure 3 [40]. Each node takes in information from the previous layer, multiplied by weights that are adjusted when the neural networks trains on data and adding a bias term, aiming to adjust these weights until the network can approximate a function that outputs a certain $\vec{y}$ from a set of inputs $\vec{x}$ [40]. Neural networks are flexible models and can be modified and optimized in a very large number of ways, including their structure, learning procedure and optimization algorithm [40]. This makes neural networks both excellent for solving complex problems, as well as notoriously difficult to use[45].
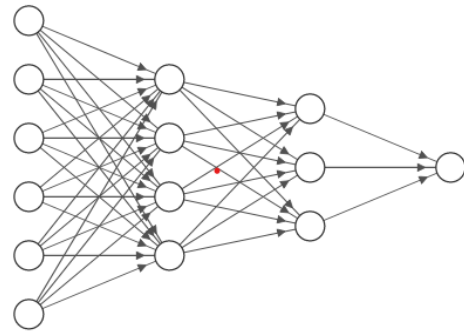
Input Layer ∈ ℝ⁶   Hidden Layer ∈ ℝ⁴ Hidden Layer ∈ ℝ³ Output Layer ∈ ℝ¹

Figure 3: Basic illustration of a neural network containing two hidden layers, six input nodes and one output node in a cone shape. Illustration created in NN SVG

5. Performance Metrics

To evaluate the prediction of a model, different metrics can be used depending on the target variable. For regression problems, χ^2, RMSE and FOM, given in Equation 31, 32 and 33 respectively can be used in the same way as for curve fitting. Classification problems on the other hand, require their own metrics to evaluate predictions on discrete variables. For classification problems where the classes contain an equal number of members in each class, Accuracy, calculated as,

$$Accuracy = \frac{\text{Total number of correct predictions}}{\text{Total number of predictions}}$$
(42)

can be used [40]. However, when there is class imbalance, meaning that the number of members of each class is not equal, other metrics are more appropriate, since accuracy can inflate the performance of a model that is performing poorly if one class only has a few members [46]. The f1-score is one metric that can be used on imbalanced classes consisting of two components, Precision, defined as

$$Precision = \frac{\text{\# of True positives}}{\text{\# of True Positives} + \text{\# of False Positives}}$$
(43)

where True Positives (TP) are samples that were correctly classified as positive and False Positives (FP) are negative samples incorrectly classified as

positive [40] [46]. The other part of the f1-score is Precision, defined as

$$Precision = \frac{\text{\# of True Positives}}{\text{\# of True Positives} + \text{\# of False Negatives}} \tag{44}$$

where False Negatives (FN) are samples classified as negative when they belonged to the positive class. The F1 score is a combination of these two metrics, given by the equation

$$F1 = 2 \times \frac{Precision \times Recall}{Precision + Recall} \tag{45}$$

which gives a more balanced evaluation of imbalanced classification performance [46]. F1-score can be directly compared to accuracy, since it reduces to the same metric when the classes are balanced.

III.   MATERIALS AND METHODS

The workflow of analysis and modeling followed an iterative method of experimentation and improvement. The general pipeline is depicted in Figure 4.
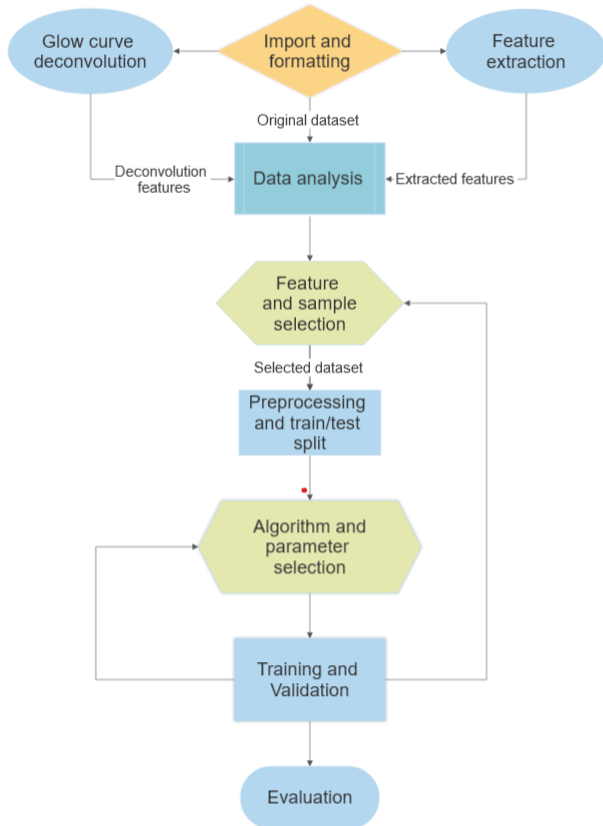

Figure 4: Flowchart depicting the data handling and prediction pipeline.

The first step of the process is not depicted in Figure 4 and is the diligent work completed at the University of Oslo (UiO) and Aarhus University (AU) to produce the required samples, irradiate them in varying positions, measure each TLD response and compile the results into the data that is used in the present work.

A.   Data collection

The first step in data collection was the synthesis of the samples used in the experiments. CaSO4:Tm and LTB:Cu was synthesized using a two-step solid state reaction and a precipitation method respectively, described in detail in the appendix in Figure 23 provided by Post. doc. R. Nattudurai . The synthesis methods resulted in polycrystalline samples of the substances, in pellet form.

Post. doc. Ravikumar Nattudurai and fellow master student Ivar Steen then irradiated the samples with protons and collected the TLD data at UiO. Additionally a secondary part of the data was collected from experiments conducted at AU following Nattudurai and Steen's directions.

Nattudurai and Steen then employed a TLDcube system (Freiberg Instruments GmbH, Freiberg, Germany) to measure the thermoluminescence of each sample. The TLDcube contains a thermocouple heater that heats the sample through the desired range, and a detector to register emitted photons with a reported system accuracy of $\pm$ 1 SD for multiple readings. When heating the sample, they used a linear heating rate of $5K/s$, up to a maximum temperature of $350°C$ depicted in Figure 5. The deviation between the set and measured temperature apparent in the tail end of the curve is the result of insufficient cooling, but for most purposes including ours, the glow curve is cut off at the peak of the curve, excluding the cooling stage. Since the heating rate is constant, the temperature and time are interchangeable variables with respect to the intensity of the glow curve, with a constant conversion factor of the heating rate ($5K/s$). The TLDcube system had a sampling rate of $10Hz$, which resulted in the measurement reaching the peak temperature after 660 points, defining the number of discrete points in each glow curve.
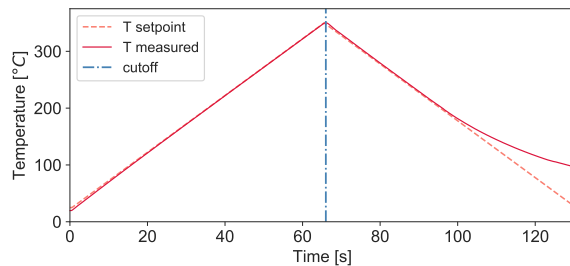

Figure 5: The employed heating curve, showing the setpoint of the heater, the measured temperature and the cutoff between heating and cooling.

B.   Data Structure

Two datasets were available, one from AU and one from UiO. The dataset from UiO consisted of 145 samples, where 67 are CaSO4:Tm and 78 are LTB:Cu. The samples were irradiated at different doses ranging from 0.34 Gy to 3.2 Gy. Most importantly, the samples were irradiated with protons at two positions in the proton beam. For CaSO4:Tm, 35 samples irradiated in position 1 (P1) and 32 in position 2

(P2). For LTB:Cu, 29 samples were irradiated in P1, and 39 in P2.

The dataset from AU consisted of 48 samples where 24 were of LTB:Cu and 24 were of CaSO4:Tm. Of the 24 samples of each substance, there was an even distribution over four positions (2a, 1a+3a, 1b, 1c), resulting in 6 samples in each position for each substance.

Each position for both datasets had an associated LET value that can be found in Table I. The LET values of the positions recorded in the experiments at AU were calculated from Monte Carlo simulations completed at AU, while the values of the positions at UiO were estimates provided by E. Malinen from Monte Carlo simulation results presented in a paper using equivalent positions and proton energies by J. Dahle , E. Malinen et al. [30]. Figure 6 shows an illustrations of the positions in the dose distribution of the proton beam. The proton energies from the UiO experiment are presented in the table, while the AU energies are not determined for each position, but lie in the range of $70 - 220 MeV$.

Table I: Positions and corresponding LET. Proton energy and LET values for P1 and P2 were estimated from equivalent positions used in the paper by J. Dahle et al.[30], and the LET values for 2a, 1a, 1b and 1c were provided by Niels Bassler from simulations conducted in connection to the experiments at Aarhus University.

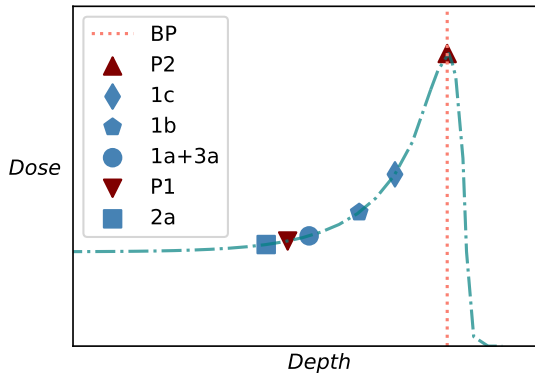| University	Position	Samples	LET [MeV/cm]	Energy [MeV]
UiO	P1	74	≈ 50	9
UiO	P2	71	≈ 270	2
AU	2a	12	47.15	70-220
AU	1a+3a	12	53.23	70-220
AU	1b	12	94.72	70-220
AU	1c	12	121.1	70-220

Figure 6: Illustration of approximate positions in Table I in relation to the Bragg Peak (BP), without scale and with arbitrary units. Blue markers signify positions irradiated at AU and maroon markers signify positions irradiated at UiO.
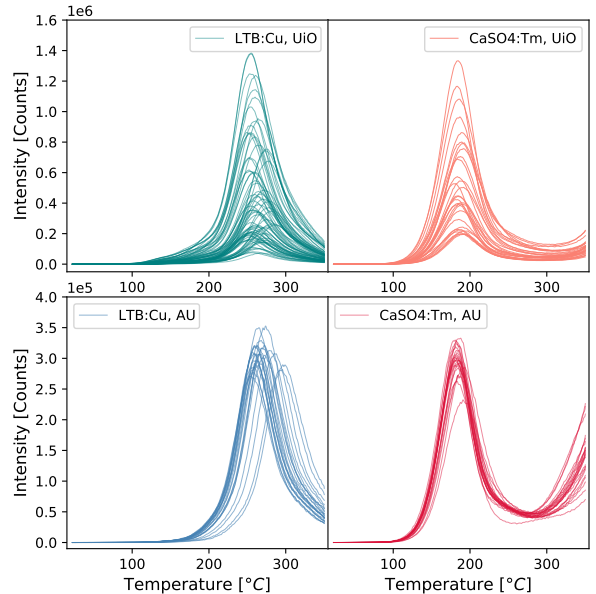

Figure 7: Plot of glow curves used in the current work, cut off at $350°C$ as illustrated in Figure 5. The two bottom plots are of glow curves from Aarhus University (AU), while the two top plots are glow curves collected from the University of Oslo (UiO).

The data consisted of the glow curves depicted in Figure 7. Each line in each plot represents a sample, where each subplot shows glow curves from a single substance and a single source. The experiment at the University of Oslo varied the dose given to the samples, which can be seen in the plots as a greater variation in the amplitude of the glow curves. In contrast, the AU samples were all irradiated at the same target peak dose of 1.0 Gy, resulting in similar amplitudes.

C. Statistical feature extraction

From the glow curves in Figure 7, statistical features were extracted for further use. The simplest features consisted of the integral of the curve known as the TL response, the maximum amplitude, the temperature of the maximum amplitude and the temperature width of the half-height, as well as the kurtosis and skew. Additional features were extracted using the

discrete derivative of the glow curves, among them the maximal amplitude, the minimal amplitude, with corresponding temperatures, as well as the integral of the differentiated curve. The features along with their corresponding label are pictured in Figure 8. The derivative of the glow curve was calculated on glow curves filtered using a Savitzky-Golay filter to reduce the noise [47]. The filter used a polynomial of order 2 and a window size of 31, found by altering the window until the high frequency noise was reduced to a reasonable level, without simplifying the underlying shape of the curve. The features illustrated in Figure 8 in addition to kurtosis and skew resulted in a total of 11 statistical features.
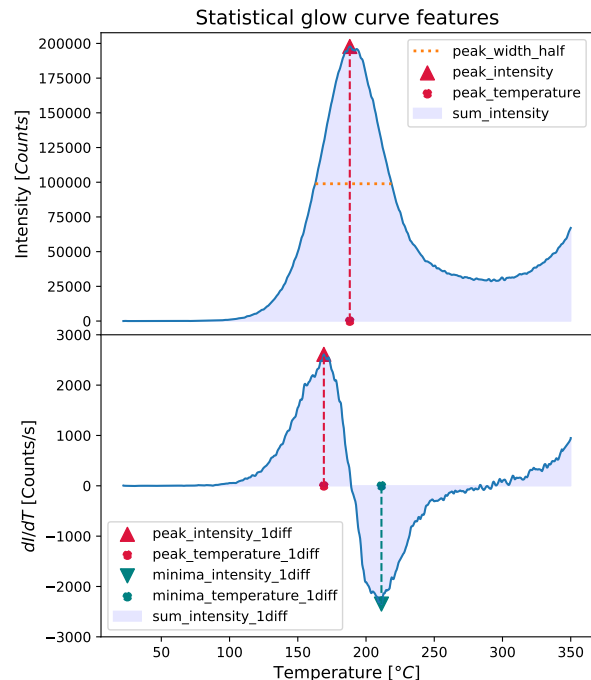

Figure 8: A sample glow curve (top), its derivative (bottom), along with markers for the extracted statistical features.

D. Glow curve deconvolution

Glow curve deconvolutions were performed using constrained Levenberg-Marquard optimization for first, second and general orders using Equations 26, 28 and 27. For each fit consisting of N peaks, a compound equation was constructed using the superposition described in Equation 29. This resulted in an equation with $N \times 3$ parameters for first and second order

equations, and $N \times 4$ parameters for the general order equation. For the first and second order equations, the parameters for each peak were Tm_i, Im_i and E_i, where Im_i is the maximal intensity of the glow peak, Tm_i is the temperature of the maximal intensity, and E_i is the energy gap from the corresponding trap to the valence band in the material. For the general order, the additional parameter b_i was extracted for each peak, which is the order of kinetics of the peak. Once this equation describing the entire glow curve had been constructed, reasonable constraints were found, to limit the search space of the LM algorithm. These constraints were very wide, only excluding negative intensities, negative energy gaps, intensities that exceeded the maximum of the glow curve, as well as peak temperatures below the starting temperature and higher than 1000 K.

Using existing literature describing the peaks presented in the theory section, as well as the residue, RMSE from Equation 32 and FOM from Equation 33 as metrics, the most reasonable peak was chosen from a fitting of the mean curve of all the samples of a certain substance. The mean curve was constructed from the UiO dataset to use as a guide. Each intensity of these curves corresponded to the mean of all samples in that position, with the aim of reducing overfitting to a certain sample. As presented earlier, the literature would indicate 2 or 4 peaks for LTB:Cu [33][34][37]. Using the mean curve, a brute force search of first, second and general order models with the number of peaks ranging from one to five was completed. Out of all of the fits for LTB:Cu, the second order model with three peaks was selected due to having the lowest RMSE, as well as looking reasonable from a visual inspection.

The model choice for CasO4:Tm was based more on literature and inspection of the glow curves, as the brute force search resulted in many fits with comparable fit metrics. CaSO4:Tm showed a main dominant peak at approximately $190°C$, slightly lower than suggested in the literature [38][39]. An additional higher temperature shoulder was also indicated, especially for higher doses, agreeing with literature [38]. A rise in intensity was also seen clearly in the highest temperature region of the CaSO4:Tm glow curves in Figure 7, and although it may possibly be caused by black body radiation, as will be discussed, it was deemed safest to fit a third peak to this rise. This was done to investigate its properties and isolate it as a component of the deconvolution, avoiding the algorithm shifting the lower temperature peaks to fit this rise. A three peak model was then also chosen for CaSO4:Tm, where second order peaks gave the best fit of the mean curve, especially of the main peak.

A model of 9 parameters as a superposition of three peaks described by Equation 28 was then selected for both substances, where each of the three peaks had three corresponding parameters E_i, Tm_i and Im_i.

When a suitable order and number of peaks had been found for the deconvolution of the mean, all samples were deconvolved. Tighter constraint were also applied before deconvolving all samples. The main constraint was on the temperature of the maximum of each peak Tm_i, where a constraint was placed around $\pm20\%$ of what had been found for the mean curve. The constraints for E_i and Im_i were looser, especially considering the UiO dataset, where the maximal intensity varied widely due to the different doses given to the samples, resulting in a wide variation in the maximum intensity of each peak Im_i.

The resulting dataset was inspected for outliers, as well as fits where the algorithm had reached the maximum or minimum values of its constraints. The parameter space indicated that it contained many local minima, varying its solutions based on both initial conditions and values of the constraints. This instability made it necessary to adjust these values until a reasonable fit within the constraints and supported by the literature was reached.

E. Data analysis and preprocessing

Once statistical features had been extracted and glow curve deconvolutions were completed, the resulting data was analysed for noise, outliers and correlations. An important job of outlier detection was in finding errors in the extraction of statistical features or deconvolution. Outisde of this, removing outliers from data is a delicate operation, especially from data that you have not collected, in a field with which you are unfamiliar. Therefore, no samples were removed, and instead the outliers were kept in mind when completing further analysis and prediction. The distributions of the samples were studied using visualizations, some of which will be presented in the results. These visualizations were important both for error detection and to get an intuition for the distribution of features, especially in relation to the different positions.

The Pearson correlation [48] was also investigated for both statistical and deconvolution features, both with other features and the target variable LET. A high absolute correlation with the target variable can be an indicator of predictive power, and a low correlation with other features can indicate unique information. The lack of any of these two qualities can signify that a feature is not useful for prediction.

Still, the variations of the correlations were large between the substances and the two datasets, and so there was no clear feature that was conclusively without value based on this analysis.

Once a satisfactory understanding of the feature distributions and correlations had been achieved, the data was preprocessed. For some methods, preprocessing was a critical element, as for PLS and PCA analysis where the data was shifted to zero-mean or standardized, or for Neural Networks where it was scaled to a 0 to 1 range, whereas for other methods it was entirely left out, or used as an additional step in attempting to improve performance.

F. Sample, feature and algorithm selection

After the extraction of different features, the main method of exploration was the selection procedure of samples, features and algorithms. Table II shows the available features after extraction. The simplest and largest set of features are the raw glow curves of the samples, where each temperature was treated as a feature, with the TL intensity as its value. This set of features by definition contains all the information of the TLD measurement. The statistical features are a set of descriptive features, aiming to concentrate the information of the data using descriptions that are quick and simple to calculate. The parameters extracted from glow curve deconvolution, and the dose, are descriptions of the data tying to physical models of the system, based on solid state physics and medical science. Each of these descriptions result in a different number of features for each sample, described in Table I, containing different representations of the information stored in the glow curves.

The AU dataset contains an equal amount of samples in the same positions for both substances, allowing a stacking of the features. For each set of features available for the AU data, one can create a new set of features that is twice the size. Each "sample" becomes a combination of two targets, LTB:Cu and CaSO4:Tm, where two samples that are from the same position but different substance are concatenated as a representation of that position.

The available samples from the six positions described in Table I were initially modelled with regression, treating the samples as a selection from a continuous LET distribution. After experimentation with regression, the data was modelled as a classification..

As a classification the positions were treated as discrete categories, and the grouping of these categories was important to investigate what split would capture differences in the samples. As the dataset from

Table II: Features available for models, where N is the number of features. Additionally, for the AU dataset, each feature can be "Stacked", resulting in a set of features of size $N \times 2$.

Features	N	Valid for	Substances
Glow curve	660	UiO and AU	LTB:Cu or CaSO4:Tm
Deconvolution	9	UiO and AU	LTB:Cu or CaSO4:Tm
Statistical	11	UiO and AU	LTB:Cu or CaSO4:Tm
Dose	1	UiO	LTB:Cu or CaSO4:Tm
Stacked	$N \times 2$	AU	LTB:Cu and CaSO4:Tm

UiO consisted of two positions, it was naturally a binary classification, while the dataset from Aarhus was on its own a multiclass classification with its four positions. The positions of the Aarhus and UiO datasets were also combined as categories in the same space. This meant assuming that the experimental conditions of the two experiments were similar enough to say that their positions could be considered classes in the same classification. This assumption allowed the samples from positions across the dataset to be grouped in different ways, opening up for an additional layer of experimentation.

The main algorithms of focus were Partial Least Squares (PLS) and Random Forests (RF), and so the selection of parameters mainly consisted of finding the optimal number of PLS components or RF trees, done through validation on a distribution of the available parameters. Additionally, investigations into PCR, Neural Networks, Support Vector Machines and clustering algorithms were conducted. For neural networks, the main exploration was on the number of layers an its architecture, as well as the learning rate and the number of training epochs. Although the investigations into these other models yielded understanding of the dataset, the full extent of the search through these algorithms will not be included for brevity, but a selection of these are included in tables in the appendix.

The metrics for the evaluation of each rmodel consisted of the RMSE, accuracy and f1-score. RMSE was used for regression predictions, accuracy was used for classification evaluation in the case where the classes were completely balanced and the f1-score

was used for classification with imbalanced classes.

G. Validation, Iteration and Evaluation

Since one part of the exploration of models included different groupings of the samples, a balanced train/test splitting had to occur after the groups had been divided to ensure equal representation in both sets. The train/test splitting was done stratified based on the target parameter, aiming for a split where the test set was 15% the size of the total data. This proportion is on the low end, but since the dataset is small, the risk of saving too much of data for testing is that the algorithm is not able to generalize on the training data. When investigating the AU dataset on its own, the test proportion was 16%, and only consisting of a single sample of each group resulting in a test set of 4 samples. The use of such a small test set is debatable, as it could completely consist of outliers or edge cases, but it still has the advantage of being unseen data, offering a less biased test of each algorithm.

The selection process leads to the validation step as seen in Figure 4. Since the number of samples was small, the performance on each combination of features and dataset of the training set was validated using Leave One Out (LOO) cross validation [49]. LOO consists of leaving one sample out of the training set, and then using it for a trial prediction. This procedure is then done for all samples, creating a prediction of all samples where none of the samples have been used for training in its own prediction. This removes any bias in train-validation splitting.

As seen in Figure 4, the variation and validation of parameters constitutes one of two loops in the workflow, where the other is the selection of features and samples. The process of selecting and validating different models is through the iterative variation of these two steps. All combinations of sample groups, features, groupings, algorithms and hyper-parameters can quickly become an unmanageable space of options that is difficult to evaluate. The exploration therefore used the analysis of the statistical and deconvolution features as a backbone, focusing in the beginning on complete sets of features (deconvolution feature/statistical features/raw curves) and later narrowing the search to models and features with high predictive performance.

Finally, after exploring the space of possible models, the ones with best performance were evaluated. Since the datasets were split between training and testing before any models were created, the best models can in the end be evaluated on unseen data, avoiding any overfitting caused by the iterative exploration itself.

H. Software Tools

Analysis, deconvolution, model construction and evaluation was done in `Python 3.7.9` . For the data management and analysis, the packages `pandas`, `scipy`, and `tensorflow` were used [50][51][52]. Glow curve deconvolution was completed with the use of `lmfit`, a package specialized for non-linear optimization problems [26]. For the building of Neural Networks and Random Forest models, `keras` and `scikit` were used respectively [53][54]. Additionally, the packages `scikit` and `hoggorm` were used to carry out PCA and PLS analysis and predictive modeling[55].

IV. RESULTS

The glow curves depicted in Figure 7 show the TLD measurement of CaSO4:Tm and LTB:Cu from the datasets gathered from UiO and AU. Firstly, an analysis of the raw data was carried out to look for patterns in noise or correlations that were present without any further processing. Thereafter, statistical features were extracted and the glow curves were deconvoluted. Finally machine learning algorithms were built and trained to predict LET from raw curves, statistical features and deconvolution parameters, both as a regression and as a classification.

A. Statistical analysis and feature extraction

1. Dose response

Since the dataset from UiO contained samples irradiated with different doses, it gave the opportunity to look at the dose response of the samples. Figure 9 shows the relationship between the dose and the TL response, calculated as the area under the glow curve. The difference in TL response of LTB:Cu between the two positions is clear in the upper plot and quantified in Table III, where the TL response was lower for P2, the position with higher LET (See Table I. The difference between these two position also increased proportionally with the dosage. In contrast, the dose response of CaSO4:Tm did not exhibit a clear difference between the positions, although the linear regression of P2 was slightly lower than P1. A commonality between the substances is that they had a linear dose response with some noise, which makes them functional dosimeters in this dose range. The TL response given in Table III is the basis for dose estimation as the proportionality constant C_p in Equation 8.

Table III: The TL response coefficients for LTB:Cu and CaSO4:Tm from the UiO dataset as slopes of the linear regressions in Figure 9. The given R^2 is of the linear regression fit in Figure 9 calculated with Equation 34.

Substance	Position	TL-response [Counts/Gy]	R^2
LTB:Cu	P1	6.2×10^7	0.99
LTB:Cu	P2	2.6×10^7	0.72
CaSO4:Tm	P1	5.6×10^7	0.97
CaSO4:Tm	P2	4.7×10^7	0.88

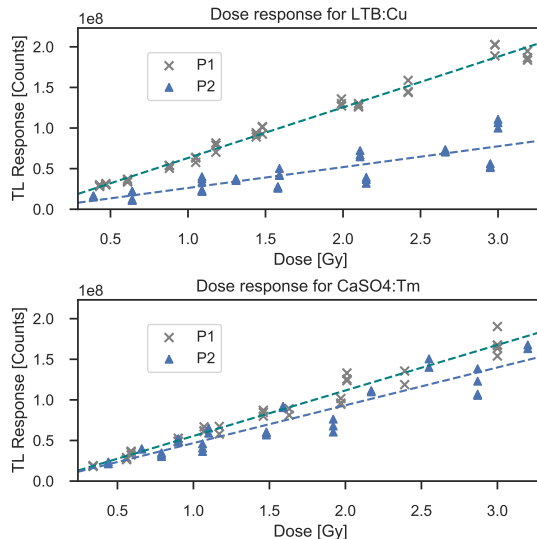
Figure 9: Dose responses of LTB:Cu and CaSO4:Tm for P1 marked with crosses and P2 marked with triangles, corresponding to positions described in Table I. For each position a linear regression was made, demarkated with dashed lines. The TL response is calculated as the area under the glow curve.

2. Noise and signals

One clear variation in the glow curves, which can be seen in the plot of the curves Figure 7, was the temperature at which the curves reach their peak. Figure 10 shows the distributions of peak temperatures for the glow curves with CaSO4:Tm in the upper plot, and LTB:Cu in the lower plot. The distribution of peak temperatures appears to be largely composed of noise, although in the lower plot of LTB:Cu the distribution of peaks for the position with a higher LET (P2) was skewed towards higher temperatures than the position with lower LET (P2). This was reversed for CaSO4:Tm, where the distribution of maximums was more skewed towards higher temperatures for P1 than for P2. No clear relationship between dose and peak temperature was observed. Looking at the distribution of peak temperatures and intensities in Figure 11, the peak temperatures were clearly separable by substance as expected. The the distribution of LTB:Cu peak intensities exhibit more spread, as was also indicated in the plotting of the glow curves in Figure 7. There was not observed any clear relationship between LET and peak temperature. The left hand plot includes data from both UiO and AU, while in the right hand plot, data from UiO was excluded due to its varying dose, causing differences in peak intensity. All samples from AU
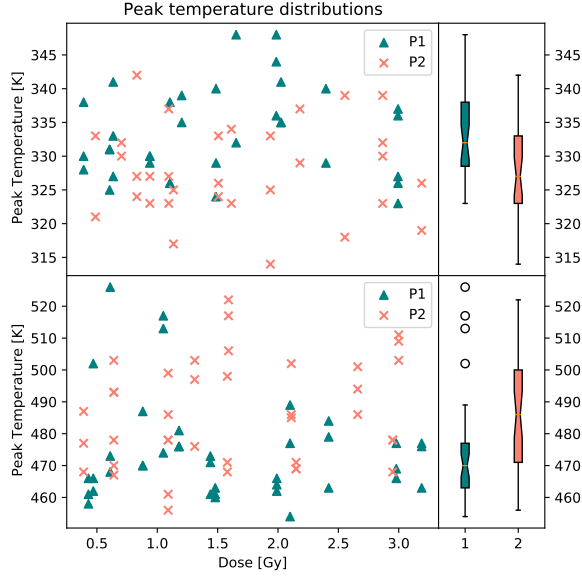
Figure 10: The distribution of the temperatures of the maxima against the received dose from the UiO data. The upper plot is of CaSO4:Tm, and the lower plot is of LTB:Cu, with triangles indicating P1 and crosses P2, see Table I. On the right side is a histogram, binning the scatterplot across the y-axis, with each position maintaining its representative color.
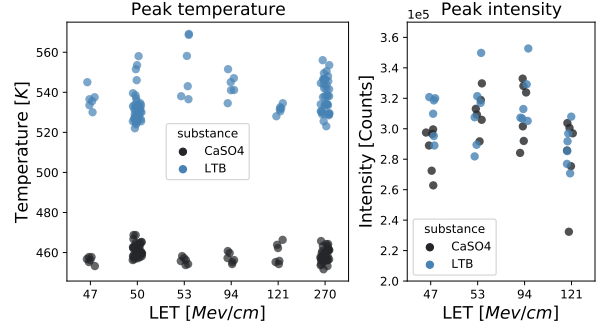

Figure 11: The distribution of maximal intensity (right) and corresponding temperature (left). The x-axis represents discrete categories corresponding to the positions of the samples in order of increasing LET (See Table I).
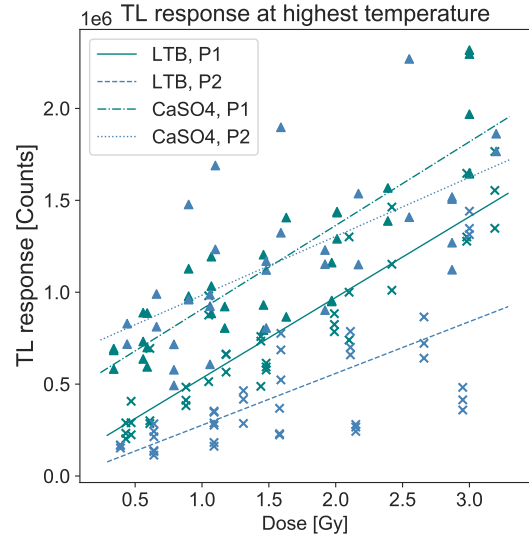

Figure 12: Sum of the intensity of the 10 highest temperature points for LTB:Cu (marked with crosses) and CaSO4:Tm (marked with triangles) samples from the UiO dataset. For each position (See Table I) and substance, a linear regression is shown as the lines of varying style.

were irradiated with the same target dose, and so as seen in the plot of the peak intensities, the two substances showed around the same sensitivity, with peak amplitudes in the same range, but still exhibiting variations of around $10 - 15\%$ for all positions, except for the clear low outlier in the $121 Mev/cm$ group of CaSO:Tm. The samples of both substances show a pattern where the peak intensity rises with LET for the three lowest groups, while the highest LET group exhibits a lower peak intensity.

Since high-temperature TLD measurements can heat materials to the range of temperatures where they exhibit black body radiation, inspecting the high temperature region can be a way of quantifying this type of noise. Figure 12 shows the response in the highest temperature region of the glow curve for the UiO data, as the sum of the intensity of the 10 highest temperature points. There was still a positive dose response shown in Table IV, although the response coefficients were lower and the noise was amplified shown in the higher R^2 coefficients in comparison to the responses in Figure 9. The response for this region was also higher for P1 in the case of both CaSO4:Tm and LTB:Cu, weakly indicating a difference in response based on position.

3. Statistical feature extraction

Statistical features presented extracted from the glow curves shown in Figure 8 were extracted for all samples from both dataset. Figure 13 and Figure 14 show the absolute Pearson correlation of the extracted features with each other and LET. The most striking difference between the two datasets is the large difference in the number of highly correlated features. This points to the key difference between the datasets, that

Table IV: The TL response coefficients for the 10 highest temperature points of the UiO dataset as slopes of the linear regressions in Figure 12. The given R^2 is of the linear regression fit calculated with Equation 34.

Substance	Position	TL-response [Counts/Gy]	R^2
LTB:Cu	P1	4.4×10^5	0.84
LTB:Cu	P2	2.8×10^5	0.51
CaSO4:Tm	P1	4.6×10^5	0.77
CaSO4:Tm	P2	3.2×10^5	0.42

the UiO samples were irradiated at different doses and the AU samples were not. The UiO dataset has many features that are highly correlated with each other, especially features that are highly correlated with dose. This high correlation that is seen is most likely explained by the confounding variable dose alone, since when dose increases, they al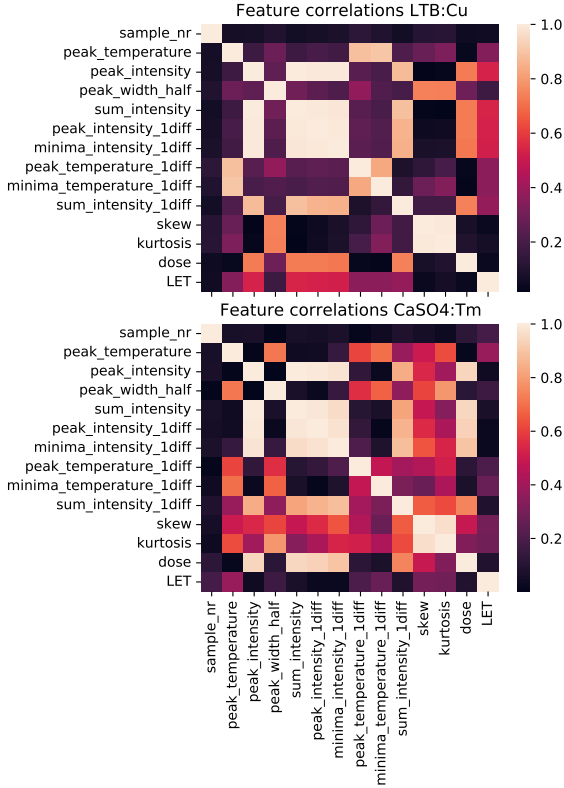l increase. One important commonality between the two datasets is that the extracted features of LTB:Cu, shown in the upper matrix of Figure 14 and Figure 13, had a higher correlation with LET, hinting at a difference in predictive power. The sample number (sample_nr) is, on the other hand, an indicator of noise. Since the sample number varies between samples of the same substance that are irradiated in the same position, with the same dose, it should ideally not have any correlation to other variables. The main difference of the correlation of this feature is between the datasets, where the dataset from AU had a higher correlation between sample number and the other extracted features, indicating sample dependent noise, with CaSO4:Tm exhibiting a higher sample number correlation than LTB:Cu. However, the CaSO4:Tm samples from the UiO experiments had the highest correlation between sample number and the target variable LET.

Figure 13: Absolute Pearson correlation matrix of extracted features shown in Figure 8, from the UiO samples. Additionally, the recieved dose is also added to the matrix.
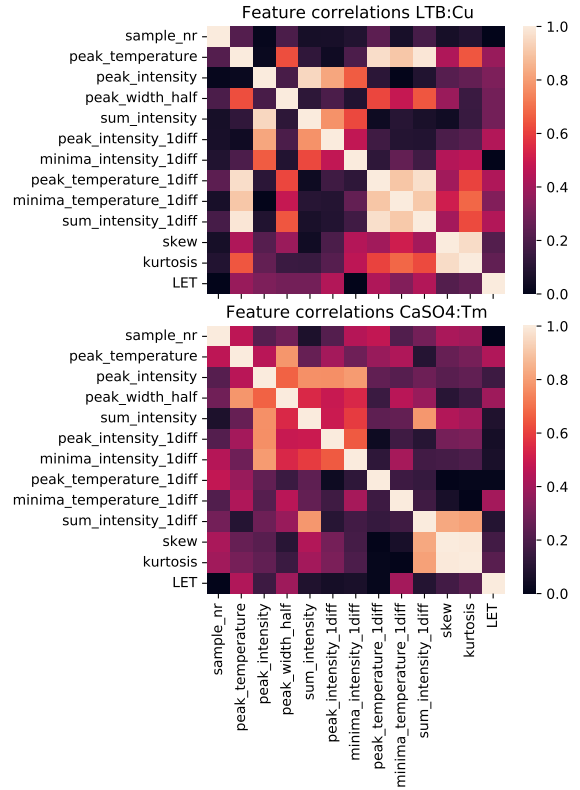

Figure 14: Absolute Pearson correlation matrix of extracted features shown in Figure 8, from the AU samples.

For the different sets and substances there are a number of features that could be discarded as they are highly correlated with each other and have low

correlation with the target. However, what features these are differs between samples and datasets. For example, looking at Figure 14 and Figure 13, the peak intensity of the first derivative of the glow curve(peak_intensity_1diff) had a relatively high correlation with LET for LTB:Cu features for both datasets, but not for features extracted from CaSO4:Tm. It also had a high correlations with the sum of intensities (sum_intensity) and the minima of the first derivative of the glow curve (minima_intensity_1diff) for both substances in the UiO dataset, while it lacked this strong correlation in the AU dataset. Since there was variation in indicated usefulness of the features between substances and dataset, none of the features were discarded before models were built, to better assess their influence.

B. Glow curve deconvolution

Figure 15 shows the deconvolution of the LTB:Cu glow curve, with the residue of the fit in a complimentary plot. The model for LTB:Cu was found through a brute-force exploration of first, second and general order models with the number of peaks ranging from one to five. A model of three second order peaks exhibited the lowest RMSE given in Table V, and showed three well separated peaks, corresponding to distinct regions of the glow curve. The exploration of these models is attached in Figure 24 in the appendix.

The deconvolution of CaSO4:Tm shown in Figure 16 exhibited a slightly higher error for the guiding mean curve, described in Table V. For the deconvolution of CaSO4:Tm, there is an especially large uncertainty attributed to the fit of the third peak due to this peak mostly being out of the temperature range of the measurement. The residue for both of these deconvolutions did not seem to be completely random which could indicate some lack of precision in the fit, but appeared in all reasonable deconvolutions and so is assumed to be noise.

Table V: Fit metrics for glow curve deconvolutions of CaSO4:Tm and LTB:Cu mean guide curves, showing the FOM and RMSE for each substance calculated with Equation 33 and Equation 32 respectively

Substance	Peaks	Order	RMSE [MeV/cm]	FOM
LTB:Cu mean	3	Second	142	0.00731
CaSO4:Tm mean	3	Second	208	0.0111

The fit metrics for the deconvolution of all the samples, described in Table VI, show that most of the de-

convolutions reached a high precision. The standard metric used to evaluating a fit as good is an FOM lower than 0.025, or in some cases lower than 0.05 [21][18]. Out of all the deconvolutions of CaSO4:Tm, five samples had a higher FOM than 0.05, as well as many samples that fall above the 0.025margin. Other than the deconvolutions for CaSO4:Tm samples from the UiO experiment, deconvolutions largely fall below the 0.025 FOM criterion with good margin, including all the deconvolutions of LTB:Cu samples.

Table VI: FOM for glow curve deconvolutions of CaSO4:Tm and LTB:Cu curves, showing the mean FOM for each substance as well as the maximum FOM. FOM calculated with Equation 33.

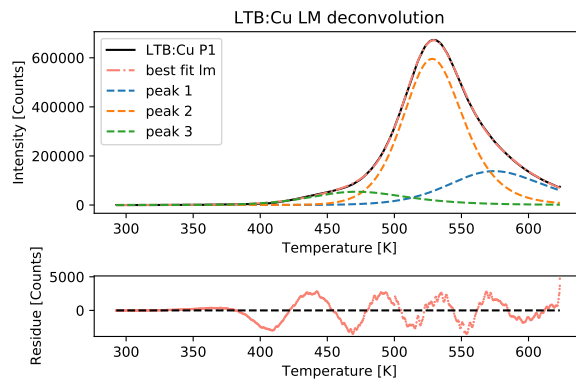| Substance	FOM Mean	FOM Max
UiO CaSO4:Tm	0.027	0.062
UiO LTB:Cu	0.00036	0.0012
AU CaSO4:Tm	0.0134	0.0277
AU LTB:Cu	0.00835	0.00978

Figure 15: Deconvolution of LTB:Cu mean curve for P1(see Table I) with three second order peaks. The difference between the experimental curve and the model fit, the residue, is shown below the deconvolution.
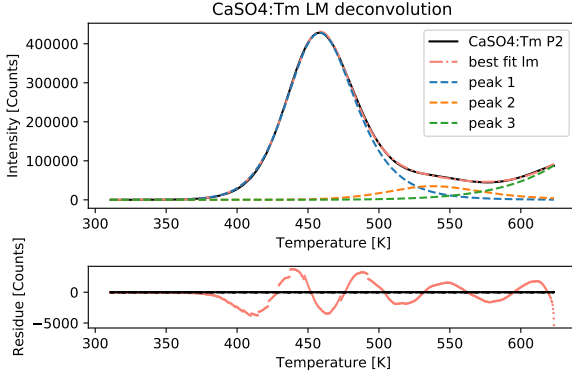
Figure 16: Deconvolution of CaSO4:Tm mean glow curve of P2 (See Table I) with three second order peaks. The error between the model curve and the experimental curve is shown in the lowest plot.

Inspecting the distributions of the energy gap E extracted from glow curve deconvolution in Figure 17 and Figure 18, one can see that for CaSO4:Tm, the energy gap attributed to the first peak, $E1$, is fairly similar for all positions, while for the energy gap attributed to the second and third peak, $E2$ and $E3$, respectively, the distributions are broader which indicates the uncertainty of the fit of those peaks. In general, LTB:Cu, shows more narrow grouping of extracted parameters for each position. Looking at Figure 18, there is also a clear difference in the extracted energy gap for the first peak ($E1$) for the positions measured at UiO (P1 and P2 in Table I) in comparison to the other positions.

C. Prediction of LET

The prediction of LET from the glow curves was first approached as a regression problem, focusing on the data collected at Aarhus due to the higher number of positions.

The investigations into regression models shown in Table VIII paints a picture of the performance of different algorithms. The best performing neural network was a cone structured network of 9 layers, with a decreasing number of nodes in each hidden layer, starting at 600 and decreasing for each layer to 1 in the output layer. This neural network, after hyperparameter optimization of the learning rate, only yielded an RMSE of $26.26 MeV/cm$ on the AU dataset glow curves. Random Forest Regression gave better results and consistency than a NN, performing especially well on the extracted statistical features. RF algorithms performed comparably at their best, but was still outperformed by PCR and PLSR in most
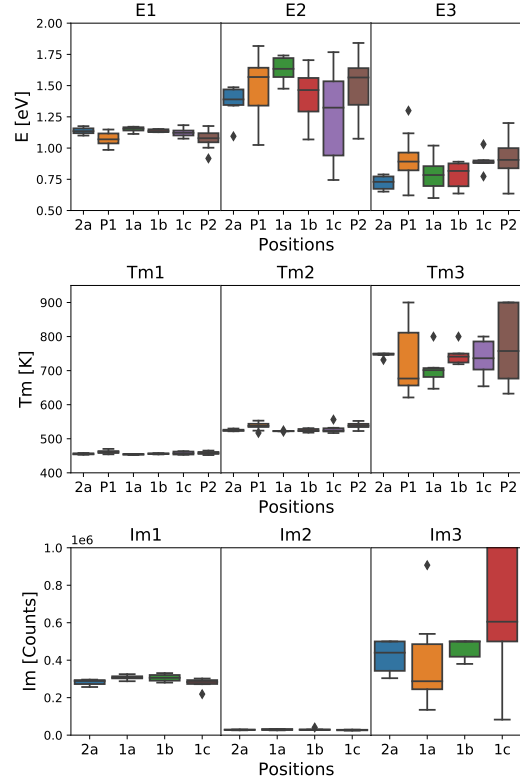

Figure 17: Distribution of parameters from deconvolution fitting of Equation 28 for three peaks showing parameters CaSO4:Cu glow curves from positions described in Table I. The UiO positions were left out of the boxplot of peak intensities Im_i, as they were measured with variable doses.

cases. PCR and PLSR gave similar performance, but PLSR needed equal or fewer components to reach the peak performance in all cases. From this it was concluded that PLS was an appropriate algorithm, eclipsing PCA based models for the problem, and so PCA based methods were dropped for further explorations.

Although many combinations and methods were tried, a reliable regression model was not achieved, with the lowest RMSE of the best model reaching $23.35 MeV/cm$, a mean relative error of 29%. The best model was built using features from the deconvolution of LTB:Cu described in Table II with a PLS regression, shown in Figure 19.

From this result it was clear that the regression model was unable to generalize the relationship between the
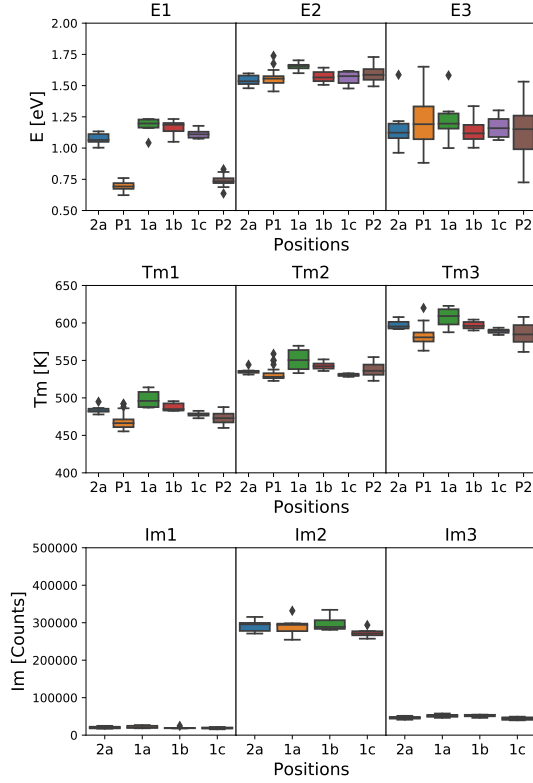
Figure 18: Distribution of parameters from deconvolution fitting of Equation 28 for three peaks showing LTB:Cu glow curves from positions described in Table I. The UiO positions were left out of the boxplot of peak intensities Im_i as in Figure 17, since they were measured with variable doses.
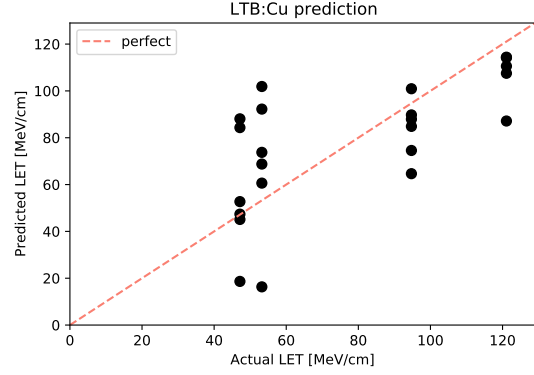

Figure 19: Regression model with the lowest RMSE of $23.35 MeV/cm$, using AU LTB:Cu samples. The red dashed line shows a perfect prediction. The PLSR model used all available components, in this case 9 which corresponds to the total number of features extracted in the deconvolution (See Table II)

data and LET. There was an especially large overlap between the two lowest LET groups of points, but a tendency for higher precision at higher LET as seen in Figure 19.

Table VII: The regression models for each algorithm with the highest performance on the AU data. RMSE was evaluated for the training set with LOO validation.

Method	Features	Marker	RMSE [MeV/cm]
NN	Glow curves	LTB:Cu	26.26
RF	Statistical	LTB:Cu	23.37
PCR	Deconvolution	LTB:Cu	23.35
PLSR	Deconvolution	LTB:Cu	23.35

Changing the approach to a classification problem yielded models with higher performance. The

first classifications were done on samples from each dataset individually. The models with the highest performance on the prediction of the four AU positions described in Table I had a validation accuracy of 0.8 and a test accuracy of 1.0, although the test set for this model only consisted of 4 samples, and so is likely not a representative selection. Two models performed equally well on this data, both using PLS classification. The first used samples of LTB:Cu, with the extracted statistical features shown in Figure 8 in conjunction with the features obtained from deconvolution. The second was a concatenation of the samples from CaSO4:Tm and LTB:Cu, using only the features extracted from the deconvolution. The second of these two predictions are shown in Figure 20. The performance on the three highest LET classes were highest, while the lowest LET position (2a) was most often misclassified as well as the class where most samples from other classes were misclassified. The highest performing NN, with 7 layers, each with 200 neurons performed worse than the PLS classification, reaching an accuracy of 0.55 using the standardized glow curves as input. A RF of 250 trees had a performance between the two, with an accurayc of 0.65.

For the dataset gathered at UiO, approaching the problem as a binary classification between P1 and P2 gave a satisfactory validation accuracy of 93% using the features extracted from deconvolution and the dose of each sample for LTB:Cu, shown in Table IX. The confusion matrix for this classification is shown in Figure 21, where the accuracy on the two classes are relatively equal. The evaluation of the model on the test set gave a lower accuracy of 87%, indicating

Table VIII: Classification models of each algorithm with the highest performance on multiclass classification of the AU positions described in Table I. The accuracy was calculated on the training data using LOO validation. The PLS classification contains both validation and test accuracy as validation/test.

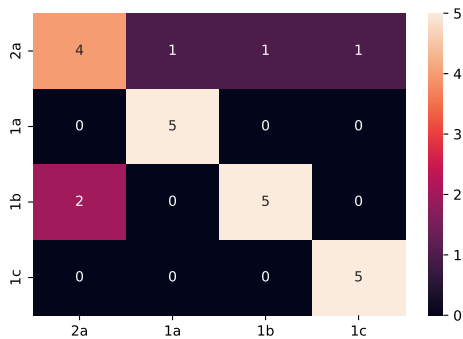| Method	Features	Substance	Accuracy
NN	Glow curves	LTB:Cu	0.55
RF	Statistical and Deconvolution	LTB:Cu	0.65
PLS	Deconvolution	LTB:Cu and CaSO4:Tm	0.8/1.0

Figure 20: Confusion matrix of multiclass classification with an accuracy of 80% of the AU glow curves where each position described in Table I was defined as a class. This prediction used stacked deconvolution features from both substances (See Table II).

some overfitting.

Table IX: Results for PLS binary classification on different groupings of positions described in Table I. Models were constructed using LTB:Cu with features extracted from glow curve deconvolution and dose received by each sample (See Table II). Validation performance is using LOO validation and test performance is on the reserved test set, using the whole training set for training. The test set for P1 vs P2 consisted of 8 samples, while the size of the second test set was 11 samples.

Classes	Validation	Test	Metric
P1 vs. P2	0.93	0.87	Accuracy
P1, 1a, 1b, 1c, 2a vs. P2	0.96	1.0	f1-score

Combining the AU and UiO datsets and predicting a classification of P2 against all other positions described in Table I gave a validation f1-score of 0.96, showing that the samples irradiated in the Bragg peak (P2) could be classified with high precision. The same model on the same classes, training on the
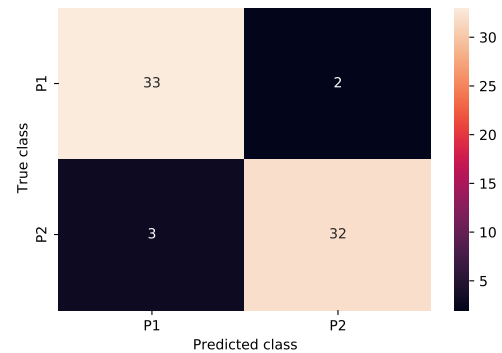

Figure 21: Confusion matrix of binary classification on UiO positions described in Table I using deconvolution features (See Table II) of LTB:Cu in addition to the dose, yielding a classification accuracy of 92.9%.

full training set and evaluating on the reserved test set gave a perfect classification, as shown in Table IX. This model used the deconvolution features in addition to the dose of the sample, removing the dose from the features significantly reduced the performance of the model to an f1-score of 0.79. Since these classes were unbalanced, with P2 having 35 member, while the combined class had 56 members, the f1 score of Equation 45 was used for evaluation. F1-score can be directly compared to accuracy, since it reduces to the same metric for balanced classes. The high performance on this classification indicates a clear difference between the glow curves irradiated in the P2 position, in comparison to the others.
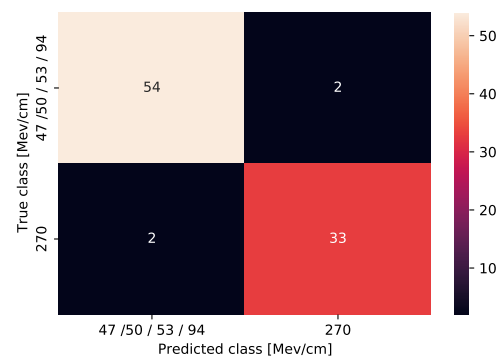

Figure 22: Confusion matrix of binary classification on UiO and AU positions described in Table I using deconvolution features (See Table II) of LTB:Cu in addition to the dose, yielding a classification f1-score of 0.96.

V. DISCUSSION

A. Overview

The core of this thesis is investigating the transfer of information from radiation to prediction. Starting with TLD readings, what information is present from irradiation and how can it be preserved? The major concern is to discern what is a relevant signal, and what is noise. Secondly, what is the optimal way of compressing the information, without losing important signals? Finally, can qualities of the original irradiation be reliably predicted from the compressed set of features?

B. Noise and Signals

One important step in the data analysis is the characterisation of clear patterns and noise in the data that will affect later feature extraction and predictive modeling. Thermoluminescence is highly dependent on material properties, where even slight changes in concentration, crystal structure or purity can have effects on the outcome [56]. This causes an inherent noise in TLD measurements, making it challenging to investigate subtle effects. Another potential source of noise stems from the fact that glow curves containing high temperature peaks may be affected by noise from black body radiation from the material or measurement system itself. As seen in Figure 12 and described in Table IV, although lower, there is still a dose dependent TL signal at the highest temperatures of the samples, but there is more noise present, making analysis of this part of the spectra difficult. There are some ways to control for this radiation, including TLD reading of two identical samples, where one is unirradiated to measure the black body radiation on its own and then subtract it from the signal of the other [57]. But such methods are unlikely to be adopted outside of scientific enquiry due to the additional equipment and work required. The temperature at which the glow curves reach their peak also exhibits a large spread without any clear pattern, as can be seen in Figure 10. This noise could be caused by many factors, and is also a critical value for the analysis of glow curves, since it is strongly connected to the energy gap variable of physical models [7]. Additionally, since the peak temperature is a parameter of the deconvolution model, the noise of each sample is propagated into the extracted parameters of the TL sample. Finding efficient ways of controlling for noise in TLD samples and eliminating the effects of black body radiation without extensive changes to the established experimental routine would be optimal, but is a difficult task.

As the current major area of use for these materials is dose estimation [2], the precision in this respect is the quality that has been optimized for when searching for new TL materials. It might therefore not be surprising that it is when investigating dose dependent effects that we get one of the easiest to find and clearest signals. Figure 9 depicting the dose response shows a linear response for both materials, where the sensitivity is comparable between the two subtances as seen in Table III, where the dose response coefficients are both on the order of 10^7. In this signal is also where we find the clearest difference between the positions of the UiO dataset (See Table I). The dose response shows a clear difference between the low LET position (P1) and the high LET position (P2). This is an important finding in itself, as it shows that TLD measurement devices irradiated in different depths of the beam, give different TL readings for the same dose. It also shows that an increase of LET is connected to a decrease in response, which is slightly counter intuitive. This difference is not seen in the dose response of CaSO4:Tm, which indicates that less information is transferred to the TL reading about the beam placement of the sample for this substance. For standard dosimetry application, this difference in TL response based on measurement depth found in LTB:Cu, which has not been found in the reviewed literature, is an unwanted quality for simple dose measurements since it creates an additional factor that has to be taken into consideration.

C. Feature extraction

The task of feature extraction is to compress the information present in the data into a smaller number of features, while retaining the important information. The key to a successful feature extraction is determining what information is important to extract. This is again dependent on what task one wants to complete. It is therefore often tricky to evaluate whether the extracted features are a sufficient representation of the dataset without evaluating them in the specific task one has chosen them for.

For the statistical features shown in Figure 8, the main evaluation outside of model testing was the Pearson correlations shown in Figure 14 and Figure 13. The most important correlation, pointing to predictive power, was the correlation with the target variable, LET. The higher correlation between the statistical features of LTB:Cu and LET gave an indication that the samples of LTB:Cu would be a better predictor of LET, before any models were built. The high correlation between features correlated with

dose and LET in LTB:Cu, also hinted at the relationship between position and dose response shown so clearly in Figure 9. This extraction not only served the purpose of creating a set of features to be used for constructing predictive models, but gave a deeper understanding of how the different expressions of the glow curve were connected.

The second method to distill the information in the TLD reading was glow curve deconvolution. The basis for this method lies in the understanding of the physical mechanics of thermoluminescence. This offers some assurance of the ability to extract important information relating to the TL sample, as there is a large volume of literature underlying the models. The major evaluation is then how this physical understanding is used to build TL models, how these models are applied through fitting to the glow curves, how accurate the TL models are on the relevant TLD data and how well they propagate the most relevant information for the construction of predictive models.

Perhaps the critical point of a glow curve deconvolution is the selection of TL model. This consists of selecting the number of underlying peaks of the glow curve, as well as what equations to use, which determine the parameters of a single peak [18]. As described earlier, there are a number of models making different assumptions, each with their own benefits and drawbacks. The difference between them lies in the necessary simplification into a model that can be practically applied. Most of them are based on the same underlying physics of the Braunlich Scharman model, described most completely by the four differential Equations 9, 10, 11 and 12. Selecting a model to use based on these equations constitutes determining or assuming something about the proportion of electrons and holes in the conduction and valence band, their rates of change, if both retrapping and recombination is radiative, as well as whether retrapping or recombination is dominant when the TL material is heated [7]. These qualities can be difficult to determine with a high certainty for TLD samples, even for materials that have a long history in TLD, as they depend on the method of synthesis, distribution of flaws in the material and doping concentrations [37] [56][7]. Without a complete knowledge of the nature of these mechanics in the investigated TL material, model selection is based on earlier literature as well as intuition gained through exploration.

The initial exploration of models, staring with a brute force search of different peaks and orders based on the mean curve of the samples from the UiO data gave a single model for LTB:Cu, that had both the lowest RMSE as well as clearly separated peaks. The situation of one large peak being interpreted as a superposition of smaller peaks risks an overly complicated deconvolution, and so clearly separated peaks are preferable, since it simplifies the model. That the initial search gave one model that had clear advantages over the other made the choice of model for deconvolution of samples of LTB:Cu relatively simple, while the choice for CaSO4:Tm required more consideration.

Since the search for models through brute force did not yield one clear preference, the choice of model for CaSO4:Tm was based mostly on a combination of earlier literature and judgement through visual inspection. The dominant peak of CaSO4:Tm had a very good fit to the second order model, as seen in Figure 16, which combined with the clear presence of a shoulder, which was also supported by the literature, led to the choice of a second order model with three peaks [38]. For CaSO4:Tm in particular, the choice of three peaks lead to a high temperature peak that was largely outside the range of measurement. This led to a larger uncertainty in the deconvolution parameters extracted, as can be seen i Figure 17, as well as an increased uncertainty in drawing any conclusions about the physical qualities of the trap associated with this peak, considering the increased noise, likely from black body radiation seen in Figure 12. However, a deconvolution without this peak would risk the LM algorithm reducing its precision of the other peaks in the glow curve to fit the intensity of the high temperature rise, it was then seen as preferable to fit a third peak, keeping its uncertainty in mind. Another method that could have been used was to cut out the high temperature region entirely, although that would create a challenging judgement of where this border is best put, as well as risk the loss of important information that could be of later use to the predictive models.

One exploration that could have been considered more closely, was the option of a different model for each peak. The dominant CaSO4:Tm peak fits very well to a second order model, indicating the dominance of retrapping, but this is difficult to claim for the second and third peaks. Ending up with a model of the same order with an equal number of peaks for both materials was coincidental, but convenient in further analysis, as it offered a more similar comparison between the substances through an equal number of features.

Glow curve deconvolution seems like a useful way of analysing dosimetry samples, but there is significant uncertainty connected to the accuracy of the parameters that are extracted. It is simple to find a deconvolution that fits a single sample, but when studying distributions of samples it is clear that the noise involved in TLD measurements is affecting the result, or the methods used are not as physically pre-

cise as one might assume. There are, for each sample and position, multiple deconvolutions that would be considered by many as a valid fit of the curve. How one chooses a fit must then be based on literature and a certain amount of intuition. Removing this subjective part of the deconvolution would be optimal, and finding ways to support the deconvolution with additional analysis or measurements would be helpful in increasing the precision of determining these parameters.

As presented earlier, methods like the initial rise method, triple point method and Hoogenstraads method, attempt to simplify the calculation of the energy gap, but these also have drawbacks and specific requirements of the data [19][20]. Models that use more complex physical interpretations, making fewer assumptions can also be applied, but when increasing the number of parameters in the equation, both computational requirements and the space of local minima increases.

D. LET predictions

As seen in Figure 20, the classification of the four groups of samples in the AU dataset was possible to a certain degree, giving an overall LOO validation accuracy of 80 %. The low LET groups were especially hard to discern in the classification, this can also be seen in the regression, where the groups with the lowest LET have a larger overlap with the other groups. The classification of the four AU groups in Figure 20 is also the only model that performed best using samples from CaSO4:Tm in addition to LTB:Cu. The prediction on the test set gave a perfect prediction, but since the test set only consisted of 4 positions, it is likely that this is not a representative performance of unseen data. Since LOO validation is unbiased in its split and the training set consisted of 24 samples, the validation performance is likely a better description of the of the model's capability.

The results of the binary classification models in Table IX shows that separating groups of points that have a wide contrast of LET values can be done with fair precision, while points that have comparable LET values are harder for the model to differentiate. This might be caused by the inherent noisiness of the data, limiting the detection of small differences that might be present. The high performance of the algorithms on separating the position located in the Bragg peak (P2), as well as the tendency for higher regression precision towards higher LET seen in the regression predictions, might also indicate that there are some LET dependent effects that are more visible as the LET grows. The binary classification of P2

against the rest, shown in Figure 22 demonstrates that the samples irradiated in position P2 contain some uniqueness that can be modeled. This is especially promising since there are samples from the UiO dataset in both classes, which excludes the option that the algorithm is simply separating datasets. Combining positions in the low LET class also improves the classification accuracy on the high LET class (P2), in comparison to the P1 vs. P2 binary classification. Combining the two datasets also increased the prediction performance on unseen data to a perfect prediction. This indicates that more samples could improve the model further, since it not only improved performance, but also decreased overfitting to the training set.

Out of the different features that were extracted, the features of the glow curve deconvolution resulted in the models with highest performance for most applications, although the statistical features often performed comparably. Glow curves generally performed worse, which is likely due to the high number of redundant features. Since each point in the glow curve is very highly correlated with its neighbouring points, most of the information stored in each feature is not unique. Additionally, the computational time of using glow curves is much larger than the two smaller set of features, especially for the RF and NN algorithms. This result shows that feature extraction for models built on TLD data not only simplifies the problem, but improves the performance.

The other aspect of the model exploration, the choice of algorithm, showed that the balance between complexity and simplification was essential. Neural networks, the most complex and computationally demanding algorithm, gave the worst results. Although it is likely that with enough fine tuning, one could find a neural network architecture that would perform as well as PLS or RF, the work required to explore the search space of possible models, and to tune them, is unlikely to be worth the effort, at least for datasets of the size used in this work.

Reviewing the literature concerning the prediction of LET using glow curves shows varying degrees of success. Most studies attempt to find regression models to estimate the LET, as that is the most direct practical use. One attempt to find a correlation between peak temperature and LET with Caso4:Dy and CaF2:Tm found an increased response of the high temperature peaks to high LET radiation, but no change in peak position [58]. Another study, investigating the incidence of intermediate energy ions on TLD-100 (LiF:Mg,Ti), found a dependence on LET, but concluded that the parameter was not estimable from the glow curve [59]. One paper describing LET estimations from TLD-600 (Li:Mg, Ti)

on space stations using the Peak Height Ratio (PHR) was able to deduce LET within a 10% margin [9], this is a significantly higher performance than the mean relative error of 29% of the best regression model produced in the current work. No examples in the reviewed literature was found approaching the problem as a classification, and so no comparative result is available. Some researchers, among them Y. Horowitz, even condemn the practice of investigating LET phenomena using TLD [60], claiming that TL is a rigorous physical phenomenon and that LET is not. Though quite a bombastic statement, there is a point to be made that (from the reviewed literature) there is not much research looking rigorously at the physical mechanisms that must be in place for a connection between TLD and LET to be present.

Although a reliable regression model was not found, the high accuracy of classification indicates that there is a depth dependent effect that can be predicted. As classification in the case of PLS is a regression followed by threshold, improving classification on more groups with higher precision is the same as building a regression model. One key point is that the choice of substance is paramount in being able to create predictive models. All the models with the highest performance in this work used data from samples of LTB:Cu. For the models to work, there has to be a physical mechanism in the material that is dependent on the variable that is being predicted.

E. The physics of LET dependence

From the results in this work, the samples of LTB:Cu were the best predictors of LET. From the reviewed literature, materials showing a significant LET dependence are lithium compounds. Materials containing ^6Li have a significant cross section to thermal neutrons, where the ^6Li atoms absorb a neutron and emit α particles [61]. This reaction is present in materials which include TLD-100, TLD-600 and TLD-700 [61]. LTB also containts some part ^6Li, and has even been used to construct a neutron detector [62]. Thermal neutrons have been shown to produce high temperature glow peaks in TLD-600 and TLD-700[63]. Proton beam therapy is known to produce secondary neutrons as an additional source of irradiation [64]. The production of secondary neutrons is a phenomoenon dependent on many factors, energy and LET among them [64]. This relationship is not one seen clearly stated in the reviewed literature, but it seems likely that a factor of LET dependence seen in TLD materials containing ^6Li is caused by secondary neutrons. This mechanism could affect the dose efficiency by changing the distribution of excited electrons in the traps of the material, leading

to different peaks being exhibited in the glow curve, as has been shown in TLD-600 and TLD-700 [63]. It could also cause local saturation along the track of the primary and secondary particles, as will be discussed. The α particles produced by the absorption of neutrons by ^6Li could also affect the glow curve as they could be a secondary source of electron excitation. In contrast, CaSO4:Tm does not contain isotopes exhibiting a high sensitivity to thermal neutrons, which could be an explanation for the difference between the materials [61].

If correct, this LET dependence in these materials would only be present when irradiated with sufficient energy to produce secondary neutrons. As only photon radiation with an energy higher than 10MeV produces a considerable amount of neutrons[64], this effect would could be present in very high energy photon irradiation, but would not be seen in lower energy photon irradiation. Studying this phenomenon more closely could be done by investigating the extent of the production of secondary neutrons in proton therapy, its dependence on LET and the effect of secondary neutrons on the glow curves of TLD materials. Extending the temperature range to higher temperatures would also be practical, to measure any high temperature peaks that are above $350°C$.

Another potential LET dependent effect is the saturation of the energy track by high LET irradiation. Increased LET has in TLD-700 shown to decrease the dose relative TL response due to the saturation of energized electrons along the particle track[65]. By exciting more electrons along the particle track than there are traps within the range of the excited electrons, energy is deposited without being measured as TL when heated, causing a lower TL signal efficiency. This fits for the dose response of LTB:Cu in Figure 9, where the high LET position(P2), shows a lower dose measurement efficiency. However, for CaSO4:Tm there is no significant difference, pointing to a difference in the two materials, which could be the density of available traps. If CaSO4:Tm has a higher density of available traps, to the point where it does not reach local saturation along the beam track, then it would not exhibit a lowered response to high LET irradiation due to beam track saturation. This would only be true up to a limit, as the material must reach saturation at some finite level, and so could be tested by experimenting with higher doses..

For the peak intensity of the four positions of the AU dataset in the right plot of Figure 11, peak intensity increased with LET, up until the highest LET group. This could fit with saturation along the particle track, if local saturation starts somewhere between $94MeV/cm$ and $121MeV/cm$. However, in contrast to the difference in dose response seen in the

UiO data of Figure 9, this pattern was present for both LTB:Cu and CaSO4:Tm. This could possibly be caused by the higher energy of the protons in the AU experiment..

F.   Limitations

The main challenges of the dataset were the number of samples, distribution of positions and heating rate. As the dataset was small, many of the solutions, especially using neural networks and random forests, were unstable and exhibited a significant amount of variation. This could be somewhat limited by increasing the number of trees in the case of random forests, but would likely be decreased more effectively by increasing the number of samples. An increased amount of samples is also likely to improve the performance of the models, indicated by the highest performing models being the ones with the largest amount of samples, utilizing a combination of the AU and UiO datasets. The second challenge was the irradiation position of the samples. If one wants to construct a regression model, positions that are spread over the entire distribution of LET values, instead of distinct categories, offer a more diverse source of information to construct the models from. The last challenge connected to the dataset was the heating rate used to measure the samples, $5K/s$, which was a constraint of the equipment used to measure the TL signal. Most scientific analysis of glow curves prefer a lower heating rate, as a high heating rate can cause increased overlap between the peaks and shift the temperature of the peaks to a higher range [2]. A lower heating rate would then create more precise deconvolutions, leading to more representative features for the construction of models, as well as more precise parameters for the TL materials in question. An important challenge not connected to the data was the search for comparable work on glow curve analysis and parameter extraction in the literature. Since experiments of TLD materials vary in a myriad of ways, including material, material synthesis, radiation type, measurement methodology it is difficult to find examples for comparison. An idealistic solution to this would be a common open database of glow curves and deconvolutions, offering a lexicon of data for comparison and investigation.

G.   Further Work

For the further work of creating models to predict radiation qualities using TLD reading, there are may avenues to explore. As the building block for any good model is good data, an important path is the completion of further experiments exploring different positions, materials and energies. Another interesting possibility is a wider exploration of the processing of the glow curves, including different explorations of curve scaling, extraction of further statistical features or using machine learning techniques like autoencoding to extract reduced dimensions containing the important information. Another path is exploring the underlying physical phenomena, especially the connection between secondary neutron generation and ^6Li is worthy of interest. One option could be to test how different proportions of ^6Li in the material affect the glow curve and whether this can be seen to directly connect to the LET dependence of the material. Another path could be to study the secondary neutron production of proton radiation in TLD materials, this could contribute to the understanding of LET dependence, as well as the effect of secondary neutrons as a source of irradiation in patients. Since a physical mechanism must be present that propagates the necessary information to the data for the models to be able to make predictions, the most essential work is perhaps identifying and investigating what this physical mechanism is, and how to most efficiently use it to create better models.

VI.   CONCLUSION

Based on the findings in this thesis, using TLD materials to predict LET with these methods in a way that is practical in the day-to-day operation of proton therapy facilities or space applications is still impractical at best. However, the effect of variance in LET on the response of TLD materials is important in accurately understanding the TLD readings from materials already widely in use. The significantly lower dose response of samples of LTB:Cu irradiated in the Bragg Peak in comparison to before it, has impacts for the interpretation of TL readings of dosimeters based on this material. That a classification model can separate samples irradiated in four different regions with a validation/test accuracy of 0.8/1.00, and differentiate between samples irradiated in and outside of the Bragg Peak with a validation/test f1 score of 0.96/1.00 shows that there is a difference that can be modeled in the readings of these positions, and a promising indication that future models can be built to determine these parameters more finely. It is however clear that there has to be an underlying physical mechanism that transfers the information about the LET in a way that is stored in the material and can be predicted by the models. It might therefore be most beneficial to investigate the physical mechanism that underlie the LET dependence seen in these results, to gain information about how to

gather data to construct high performing models.

VII.   ACKNOWLEDGEMENTS

[1] Hui Liu and Joe Chang. Proton therapy in clinical practice. *Chinese journal of cancer*, 30:315–26, 05 2011.

[2] Kron T. Thermoluminescence dosimetry and its applications in medicine–part 1: Physics, materials and equipment. *Australasian physical and engineering sciences in medicine*, 17:175–199, 1994.

[3] Hardev Virk. History of luminescence from ancient to modern times. 02 2014.

[4] Y. Horowitz, R. Chen, L. Oster, and I. Eliyahu. Thermoluminescence theory and analysis: Advances and impact on applications. In John C. Lindon, George E. Tranter, and David W. Koppenaal, editors, *Encyclopedia of Spectroscopy and Spectrometry (Third Edition)*, pages 444–451. Academic Press, Oxford, third edition edition, 2017.

[5] Marie Curie. Recherches sur les substances radioactives. *L'ecole polytechnique de Paris*, 1904.

[6] John Turton Randall, Maurice Hugh Frederick Wilkins, and Marcus Laurence Elwin Oliphant. Phosphorescence and electron traps - i. the study of trap distributions. *Proceedings of the Royal Society of London. Series A. Mathematical and Physical Sciences*, 184(999):365–389, 1945.

[7] (Reuven) Chen and Y Kirsh. *Analysis of thermally stimulated processes*. International series in the science of the solid state. Pergamon Press, 1st ed. edition, 1981.

[8] Ana Vaniqui, Femke Vaassen, Dario Di Perri, Daniëlle Eekers, Inge Compter, Ilaria Rinaldi, Wouter van Elmpt, and Mirko Unipan. Linear energy transfer and relative biological effectiveness investigation of various structures for a cohort of proton patients with brain tumors. *Advances in Radiation Oncology*, 8(2):101128, 2023.

[9] W. Schöner, Norbert Vana, Manfred Fugger, and E. Pohn. The peak-height ratio (htr)method for let-determination with tlds and an attempt for a microdosimetric interpretation. 01 1997.

[10] Kevin Kröninger, Florian Mentzel, Robert Theinert, and Jörg Walbersloh. A machine learning approach to glow curve analysis. *Radiation Measurements*, 125, 02 2019.

[11] Florian Mentzel, Evelin Derugin, Hannah Jansen, Kevin Kröninger, Olaf Nackenhorst, Jörg Walbersloh, and Jens Weingarten. No more glowing in the dark: How deep learning improves exposure date estimation in thermoluminescence dosimetry. *Journal of Radiological Protection*, 41, 08 2021.

[12] Claudio Furetta and George Kitis. Models in thermoluminescence. *Journal of Materials Science*, 39:2277–2294, 04 2004.

[13] Claudio Furetta. *Handbook of Thermoluminescence*. WORLD SCIENTIFIC, 2003.

[14] P. Bräunlich and A. Scharmann. Approximate solution of schön's balance equations for the thermoluminescence and the thermally stimulated conductivity of inorganic photoconducting crystals. *physica status solidi (b)*, 18(1):307–316, 1966.

[15] G F J Garlick and A F Gibson. The electron trap mechanism of luminescence in sulphide and silicate phosphors. *Proceedings of the Physical Society*, 60(6):574, jun 1948.

[16] V. Maxia. Nonequilibrium thermodynamics of the thermoluminescent process. *Phys. Rev. B*, 17:3262–3268, Apr 1978.

[17] Eduardo G. Yukihara, Stephen W.S. McKeever, Claus E. Andersen, Adrie J.J. Bos, Ian K. Bailiff, Elisabeth M. Yoshimura, Gabriel O. Sawakuchi, Lily Bossin, and Jeppe B. Christensen. Luminescence dosimetry. *Nature Reviews Methods Primers*, 2(1), 2022.

[18] G Kitis, J M Gomez-Ros, and J W N Tuyn. Thermoluminescence glow-curve deconvolution functions for first, second and general orders of kinetics. *Journal of Physics D: Applied Physics*, 31(19):2636, oct 1998.

[19] M. Rasheedy. Method of hoogenstraaten as a tool for obtaining the trap parameters of general-order thermoluminescence glow peaks. *Radiation Effects and Defects in Solids*, 160:383–390, 09 2005.

[20] M Kundu, S Bhattacharyya, M Karmakar, and P S Majumdar. Three-Point area method for thermoluminescence glow curve analysis and its application to the glowpeak of K2SRP2O7:PR. *Radiation Protection Dosimetry*, 193(3-4):247–258, 05 2021.

[21] H.Garo Balian and Nelson W. Eddy. Figure-of-merit (fom), an improved criterion over the normalized chi-squared test for assessing goodness-of-fit of gamma-ray spectral peaks. *Nuclear Instruments and Methods*, 145:389–395, 1977.

[22] Colin Lewis-Beck and Michael Lewis-Beck. *Applied regression: An introduction*, volume 22. Sage publications, 2015.

[23] Rene Andrae, Tim Schulze-Hartung, and Peter Melchior. Dos and don'ts of reduced chi-squared, 2010.

[24] Henri P. Gavin. Thermoluminescence (tl) kinetics of caso4 and lif standard materials: a comparative study. *Department of Civil and Environmental En-*

gineering, 2022.

[25] Åke Björck. *Numerical Methods for Least Squares Problems*. Society for Industrial and Applied Mathematics, 1996.

[26] Andrew Nelson et al. Matt Newville, Renee Otten. lmfit: Non-linear least-squares minimization and curve-fitting for python, April 2023.

[27] Hasan Murshed. Chapter 3 - radiation biology. In Hasan Murshed, editor, *Fundamentals of Radiation Oncology (Third Edition)*, pages 57–87. Academic Press, third edition edition, 2019.

[28] A. Fasso' A. Ferrari, P.R. Sala and J. Ranft. Fluka: a multi-particle transport code. *CERN-2005-10*, 10 2005.

[29] Wei Deng, Yunze Yang, Chenbin Liu, Martin Bues, Radhe Mohan, William W. Wong, Robert H. Foote, Samir H. Patel, and Wei Liu. A Critical Review of LET-Based Intensity-Modulated Proton Therapy Plan Evaluation and Optimization for Head and Neck Cancer Management. *International Journal of Particle Therapy*, 8(1):36–49, 06 2021.

[30] M. Zahedifar, L. Karimi, and M.J. Kavianinia. Thermoluminescence general-order glow curve deconvolution function with continuous distribution of activation energies. *Nuclear Instruments and Methods in Physics Research Section A: Accelerators, Spectrometers, Detectors and Associated Equipment*, 564(1):515–520, 2006.

[31] Gholamhossein Izadi Vasafi, Mohammad Mehdi Firoozabadi, and Mahdi Ghorbani. Detailed analysis of dose difference in using water as tissue-equivalent material in 252cf brachytherapy. *Reports of Practical Oncology Radiotherapy*, 24(6):660–666, 2019.

[32] Mutsuo Takenaga, Osamu Yamamoto, and Tadaoki Yamashita. Preparation and characteristics of li2b4o7 : Cu phosphor. *Nuclear Instruments and Methods*, 175(1):77–78, 1980.

[33] Mutsuo Takenaga, Osamu Yamamoto, and Tohru Yamashita. A new phosphor li2b4o7: Cu for tld. *Health physics*, 44 4:387–93, 1983.

[34] Swarnapriya Thiyagarajan, M. A. Vallejo, P. Cerón, C. Gomez-Solis, C. Wiechers, E. Montes, R. Navarro, and M. A. Sosa. Thermoluminescence of cu-doped li2b4o7+ptfe annealed by graphene exposed to x-rays and gamma radiation. *Journal of Molecular and Engineering Materials*, 08(03n04):2050005, 2020.

[35] Babita Tiwari, N.S. Rawat, D.G. Desai, S.G. Singh, M. Tyagi, P. Ratna, S.C. Gadkari, and M.S. Kulkarni. Thermoluminescence studies on cu-doped li2b4o7 single crystals. *Journal of Luminescence*, 130(11):2076–2083, 2010.

[36] Vibha Chopra, Lakhwant Singh, and S P Lochab. Thermoluminescence characteristics of gamma irradiated li2b4o7:cu nanophosphor. *Nuclear Instruments and Methods in Physics Research Section A: Accelerators, Spectrometers, Detectors and Associated Equipment*, 717:63–68, 07 2013.

[37] S. Soheilian, B. Movahedi, M.N. Nasrabadi, and I. Jabbari. A different approach to fabricate nanocrystalline ltb:cu pellets with thermoluminescence response. *Radiation Measurements*, 89:14–22, 2016.

[38] Tohru Yamashita, N. Nada, H. Onishi, and Saburo Kitamura. Calcium sulfate activated by thulium or dysprosium for thermoluminescence dosimetry. *Health physics*, 21 2:295–300, 1971.

[39] A.S. Deshpande, N.S. Dhoble, S. C. Gedam, and S. J. Dhoble. Thermoluminescence (tl) kinetics of caso4 and lif standard materials: a comparative study. *Recent Research in Science and Technology*, 4(8), 2012.

[40] S. Raschka, V. Mirjalili, and an O'Reilly Media Company Safari. *Python Machine Learning - Third Edition*. Packt Publishing, 2019.

[41] Ian T. Jolliffe and Jorge Cadima. Principal component analysis: a review and recent developments. *Philosophical Transactions of the Royal Society A: Mathematical, Physical and Engineering Sciences*, 374(2065):20150202, 2016.

[42] Dr. S. Jackson and Dr. K. Perrakis. Machine learning: Chapter 6 principal component regression, 2023.

[43] Michael Haenlein and Andreas Kaplan. A beginner's guide to partial least squares analysis. *Understanding Statistics*, 3, 11 2004.

[44] Paul Geladi and Eigil Dåbakk. Computational methods and chemometrics in near infrared spectroscopy*. In John C. Lindon, editor, *Encyclopedia of Spectroscopy and Spectrometry (Second Edition)*, pages 386–391. Academic Press, Oxford, second edition edition, 1999.

[45] Xavier Glorot and Y. Bengio. Understanding the difficulty of training deep feedforward neural networks. *Journal of Machine Learning Research - Proceedings Track*, 9:249–256, 01 2010.

[46] Joos Korstanje. The f1 score, 2021.

[47] Abraham Savitzky and M. J. E. Golay. Smoothing and Differentiation of Data by Simplified Least Squares Procedures. *Anal. Chem.*, 36(8):1627–1639, July 1964.

[48] David Freedman, Robert Pisani, and Roger Purves. Statistics (international student edition). *Pisani, R. Purves, 4th edn. WW Norton & Company, New York*, 2007.

[49] Trevor Hastie, Robert Tibshirani, and Jerome Friedman. *The Elements of Statistical Learning*. Springer Series in Statistics. Springer New York Inc., New York, NY, USA, 2001.

[50] The pandas development team. pandas-dev/pandas: Pandas, February 2020.

[51] Gommers Ralf Oliphant Travis E. Virtanen, Pauli and Haberland et al. SciPy 1.0: Fundamental Algorithms for Scientific Computing in Python. *Nature Methods*, 17:261–272, 2020.

[52] Paul Barham et al. Martín Abad, Ashish Agarwal. TensorFlow: Large-scale machine learning on heterogeneous systems, 2015. Software available from tensorflow.org.

[53] François Chollet et al. Keras. https://keras.io, 2015.

[54] F. Pedregosa, G. Varoquaux, A. Gramfort, V. Michel, B. Thirion, O. Grisel, M. Blondel, P. Prettenhofer, R. Weiss, V. Dubourg, J. Vanderplas, A. Passos,

D. Cournapeau, M. Brucher, M. Perrot, and E. Duchesnay. Scikit-learn: Machine learning in Python. *Journal of Machine Learning Research*, 12:2825–2830, 2011.

[55] Oliver Tomic, Thomas Graff, Kristian Hovde Liland, and Tormod Næs. hoggorm: a python library for explorative multivariate statistics. *The Journal of Open Source Software*, 4(39), 2019.

[56] Farrington Daniels, Charles A. Boyd, and Donald F. Saunders. Thermoluminescence as a research tool. *Science*, 117(3040):343–349, 1953.

[57] Emanuel P. Manche. Differential thermoluminescence (DTL) —a new instrument for measurement of thermoluminescence with suppression of blackbody radiation. *Review of Scientific Instruments*, 49(6):715–717, 08 2008.

[58] A. S. Pradhan and A. K. Bakshi. Glow peak temperature, supralinearity and LET dependence of TLDs—correlation studies. *Radiation Protection Dosimetry*, 119(1-4):276–279, 04 2006.

[59] Guerda Massillon-Jl, Isabel Gamboa-deBuen, and María-Ester Brandan. Let and dose dependence of tld-100 glow curve after exposure to intermediate-energy ions. *Radiation protection dosimetry*, 120:341–4, 02 2006.

[60] Yigal Horowitz. The concept of let in thermoluminescence dosimetry - is it meaningful or helpful? *Radiation protection dosimetry*, 106:195–6, 02 2003.

[61] J.A. Douglas. The applications of TL materials in neutron dosimetry. *Atomic Energy Research Establishment*, 08 1978.

[62] Discrimination of neutrons and gamma rays by a neutron detector comprising a superconducting tunnel junction on a single crystal of li2b4o7. *Nuclear Instruments and Methods in Physics Research Section A: Accelerators, Spectrometers, Detectors and Associated Equipment*, 529(1):402–404, 2004. Proceedings of the Joint Meeting of the International Conference on Neutron Optics (NOP2004) and the Third International Workshop on Position-Sensitive Neutron Detectors (PSND2004).

[63] A. Triolo, M. Brai, M. Marrale, G. Gennaro, and A. Bartolotta. Study of the glow curves of TLD exposed to thermal neutrons. *Radiation Protection Dosimetry*, 126(1-4):333–336, 05 2007.

[64] Roger Antoine Hälg and Uwe Schneider. Neutron dose and its measurement in proton therapy—current state of knowledge. *The British Journal of Radiology*, 93(1107):20190412, 2020. PMID: 31868525.

[65] E.R. Benton, A.L. Frank, and E.V. Benton. Tld efficiency of 7lif for doses deposited by high-let particles. *Radiation Measurements*, 32(3):211–214, 2000.

VIII. APPENDIX

Table X: Regression results for AU data different combinations of algorithms, features and substances.RMSE was computed with LOO [49] on the four groups of the AU data (See Table I).

markers	features	RMSE	algorithm
LTB	raw curves	26.41	PLSR
CaSO4	raw curves	24.95	PLSR
LTB and CaSO4	raw curves	30.23	PLSR
LTB	decon + stat	24.71	PLSR
CaSO4	decon + stat	32.56	PLSR
LTB and CaSO4	decon + stat	29.70	PLSR
LTB	decon	23.35	PLSR
CaSO4	decon	29.73	PLSR
LTB and CaSO4	decon	27.89	PLSR
LTB	stat	29.37	PLSR
CaSO4	stat	33.02	PLSR
LTB and CaSO4	stat	30.31	PLSR
LTB	raw curves	26.94	PCR
CaSO4	raw curves	24.45	PCR
LTB and CaSO4	raw curves	28.99	PCR
LTB	decon + stat	24.62	PCR
CaSO4	decon + stat	31.34	PCR
LTB and CaSO4	decon + stat	28.99	PCR
LTB	decon	23.35	PCR
CaSO4	decon	29.14	PCR
LTB and CaSO4	decon	27.24	PCR
LTB	stat	29.72	PCR
CaSO4	stat	32.14	PCR
LTB and CaSO4	stat	29.44	PCR
LTB	raw curves	31.31	RF
CaSO4	raw curves	28.91	RF
LTB and CaSO4	raw curves	30.42	RF
LTB	decon + stat	24.86	RF
CaSO4	decon + stat	33.65	RF
LTB and CaSO4	decon + stat	26.55	RF
LTB	decon	30.73	RF
CaSO4	decon	28.93	RF
LTB and CaSO4	decon	30.09	RF
LTB	stat	23.73	RF
CaSO4	stat	34.12	RF
LTB and CaSO4	stat	24.31	RF

Table XI: Classification results for different combinations of algorithms, features and substances. Accuracy was computed with LOO [49], binary classifications were between the two groups of the UiO data, while the muliclass classifications were on the four groups of the AU data (See Table I).

markers	features	Accuracy	algorithm
LTB	raw curves	0.6500	PLS_bin_UiO
CaSO4	raw curves	0.7000	PLS_bin_UiO
LTB and CaSO4	raw curves	0.7000	PLS_bin_UiO
LTB	decon + stat	0.8000	PLS_bin_UiO
CaSO4	decon + stat	0.6000	PLS_bin_UiO
LTB and CaSO4	decon + stat	0.8500	PLS_bin_UiO
LTB	decon	0.8500	PLS_bin_UiO
CaSO4	decon	0.5500	PLS_bin_UiO
LTB and CaSO4	decon	0.6500	PLS_bin_UiO
LTB	decon - HTP	0.7500	PLS_bin_UiO
CaSO4	decon - HTP	0.7500	PLS_bin_UiO
LTB and CaSO4	decon - HTP	0.6500	PLS_bin_UiO
LTB	raw curves	0.6500	RF_bin_UiO
CaSO4	raw curves	0.6000	RF_bin_UiO
LTB and CaSO4	raw curves	0.6500	RF_bin_UiO
LTB	decon + stat	0.6500	RF_bin_UiO
CaSO4	decon + stat	0.5000	RF_bin_UiO
LTB and CaSO4	decon + stat	0.5000	RF_bin_UiO
LTB	decon	0.6000	RF_bin_UiO
CaSO4	decon	0.5000	RF_bin_UiO
LTB and CaSO4	decon	0.4000	RF_bin_UiO
LTB	decon - HTP	0.6000	RF_bin_UiO
CaSO4	decon - HTP	0.4500	RF_bin_UiO
LTB and CaSO4	decon - HTP	0.4500	RF_bin_UiO
LTB	raw curves	0.5800	PLS_multi_AU
CaSO4	raw curves	0.5000	PLS_multi_AU
LTB and CaSO4	raw curves	0.7083	PLS_multi_AU
LTB	decon + stat	0.7900	PLS_multi_AU
CaSO4	decon + stat	0.5500	PLS_multi_AU
LTB and CaSO4	decon + stat	0.6500	PLS_multi_AU
LTB	decon	0.6000	PLS_multi_AU
CaSO4	decon	0.6000	PLS_multi_AU
LTB and CaSO4	decon	0.8000	PLS_multi_AU
LTB	decon - HTP	0.6000	PLS_multi_AU
CaSO4	decon - HTP	0.3500	PLS_multi_AU
LTB and CaSO4	decon - HTP	0.4500	PLS_multi_AU
LTB	raw curves	0.6000	RF_multi_AU
CaSO4	raw curves	0.2000	RF_multi_AU
LTB and CaSO4	raw curves	0.5500	RF_multi_AU
LTB	decon + stat	0.6500	RF_multi_AU
CaSO4	decon + stat	0.5500	RF_multi_AU
LTB and CaSO4	decon + stat	0.5500	RF_multi_AU
LTB	decon	0.5000	RF_multi_AU
CaSO4	decon	0.2500	RF_multi_AU
LTB and CaSO4	decon	0.4000	RF_multi_AU
LTB	decon - HTP	0.5000	RF_multi_AU
CaSO4	decon - HTP	0.3000	RF_multi_AU
LTB and CaSO4	decon - HTP	0.3500	RF_multi_AU

Synthesis of Li$_2$B$_4$O$_7$: Cu polycrystalline material

The polycrystalline material of 0.05 mol% copper doped lithium tetraborate was synthesized using standard two step solid-state reaction method. The reactants were taken in a stoichiometric composition ratio of 0.95 mol% of lithium carbonate (99.99% pure, Sigma-Aldrich Chemical company, USA), 0.05 mol% of copper oxide (purity 99.99%, Sigma-Aldrich Chemical company, USA) and 4 mol% of boric acid (purity 99.9%, Sigma-Aldrich Chemical company, USA). In the first step, the stoichiometric mixture was taken in a porcelain crucible and was kept at a temperature of 400 °C for 6 h to eliminate the absorbed water content present in the mixture. After cooling to room temperature, the mixture was once again well-grounded using an agate mortar. In the second step, the product was sintered at 750 °C for 3 h to eliminate carbon-di-oxide present in the mixture and for the formation of Li$_2$B$_4$O$_7$: Cu compound. The synthesis chemical reaction is given by the following equation,

$$Li_2CO_3 + 4H_3BO_3 + 0.05CuO \rightarrow Cu_{0.05} : Li_2B_4O_7 + 6H_2O \uparrow + CO_{2.05} \uparrow$$
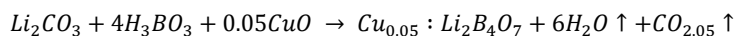
Synthesis of CaSO$_4$: Tm polycrystalline material

Calcium sulfate doped with thulium (Tm^{3+}) was prepared by the co-precipitation method. This method is a classic and simple approach for the synthesis of nanophosphor substances. The process involves the precipitation of salt (such as sulfates, nitrates and chlorides) in aqueous solutions by adding a base such as (NH$_4$)$_2$SO$_4$, NaOH, or similar. Here, CaCl$_2$, (NH$_4$)$_2$SO$_4$ and TmCl$_3$ were used as the starting ingredients. CaSO$_4$: Tm was prepared by dissolving CaCl$_2$ (99.9% trace metals basis, Sigma-Aldrich Chemical company, USA) with TmCl$_3$ (99.99% trace metals basis, Sigma-Aldrich Chemical company, USA) and (NH$_4$)$_2$SO$_4$ ($\geq$99.0% purity, Sigma-Aldrich Chemical company, USA) in deionized water. When the two solutions were mixed together, the CaSO$_4$: Tm nanophosphors co-precipitated. The clear liquid with chlorine content on the top of the precipitates was removed. The precipitates were allowed to settle

Figure 23: Procedure for TLD sample synthezis.
Provideed by Post. Doc Ravikumar Nattudurai at the
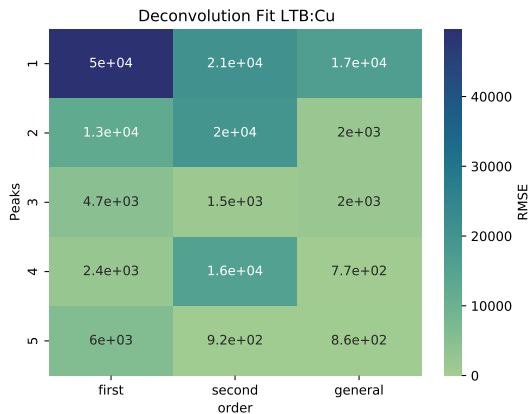*University of Oslo.*

Figure 24: Squared RMSE for the exploration of deconvolution fits of LTB:Cu with models of different order and with a different number of peaks.
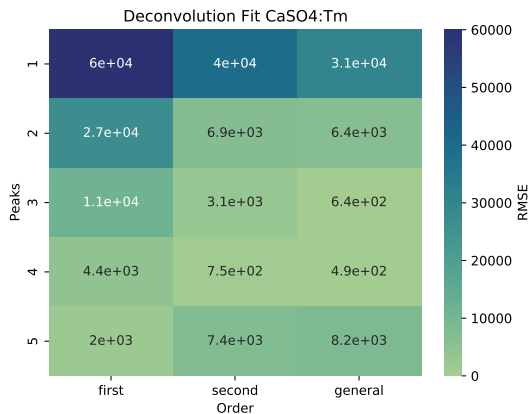

Figure 25: Squared RMSE for the exploration of deconvolution fits of CaSO4:Tm with models of different order and with a different number of peaks.
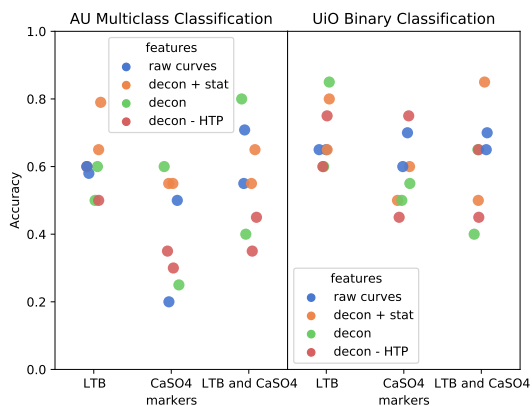

Figure 26: Classification performance of explored models described in Table XI using different markers and different features, each combination of these two variables contain points for two algorithms, RF regression and PLS classification.
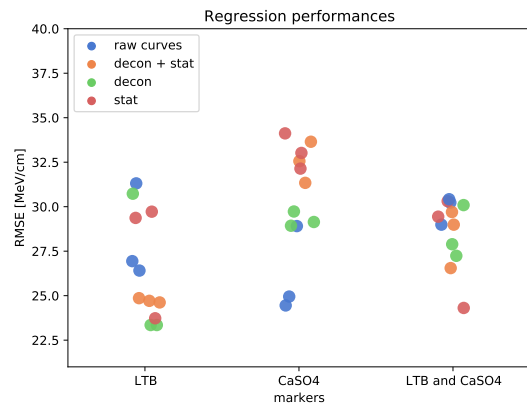

Figure 27: Regression performance of explored models described in Table X using different markers and different features, each combination of these two variables contain points for three algorithms, RF classification, PLSR and PCR.

Table XII: Investigation into neural network classification and regression on the AU dataset using samples of LTB:Cu.

layers	Task	Performance	Architecture
9	Classification	Accuracy 0.50	Cone
7	Classification	Accuracy 0.55	Linear
6	Regression	RMSE 34.57 MeV/cm	Cone
8	Regression	RMSE 33.18 MeV/cm	Linear
8	Regression	RMSE 26.26 MeV/cm	Cone